*Electronic Supplementary Information (ESI)*

# Mode of Electroactive Species Evolution from $Fe_3X_4$ (X= Se, S, O): Guideline from the Redox Chemistry of Chalcogen Anions

Avinava Kundu, Simmi Gautam and Biswarup Chakraborty*

Department of Chemistry, Indian Institute of Technology Delhi, Hauz Khas, 110016, New Delhi, India

***cbiswarup@chemistry.iitd.ac.in**

---

**Table of Contents**

## Experimental Section

### Materials

$FeCl_3.6H_2O$, $N_2H_4.H_2O$, and KOH were purchased from Central Drug House (CDH), India. $Fe(acac)_3$ was purchased from Sigma-Aldrich. The sulfur powder was purchased from Fisher Scientific. Selenium powder 100 mesh (99.5%) was purchased from Sigma Aldrich. $ZnCl_2$ (98.0%) was purchased from TCI Chemicals. All the chemicals purchased were directly used without any further purification. The nickel foam was purchased from RVL Scientific, India, and used after washings as explained below. The Glassy Carbon electrode and Hg/HgO as used as working and reference electrodes respectively, was supplied by CHI, India. Nafion 117 containing solution was purchased from Sigma Aldrich.

### Preparation of materials

***Synthesis of $Fe_3Se_4$.*** $Fe_3Se_4$ was synthesized by a pre-reported method with slight modifications. In a three-neck round bottom flask (250 mL) fixed with a condenser, 35 mL of oleylamine was taken. Then, the set-up was held at 393 K for 1 h to remove dissolved impurities under the Ar atmosphere. The $Fe(acaac)_3$ (0.53 g) and Se powder (0.158 g) precursors were added at 393 K under stirring conditions and then the temperature was raised to 473 K for another 1 h. After holding the temperature at 473 K, the temperature was again raised to 573 K for another 1 h. Finally, the reaction temperature was dropped to room temperature and the reaction was quenched with 2-propanol (25 mL). The $Fe_3Se_4$ particles were then collected by washing three times with a mixture of hexane and 2-propanol (2:3) at 5000 RPM. The final powder sample was collected by drying at 60 $^oC$ for 2 h.

***Synthesis of $Fe_3S_4$.*** $Fe_3S_4$ used herein was prepared by a pre-reported method without any modifications.[1]

***Synthesis of $Fe_3O_4$.*** $Fe_3O_4$ used herein was prepared by a pre-reported method without any modifications.[1]

***Synthesis of ZnSe.*** Anhydrous $ZnCl_2$ (0.19 g) was dissolved in 30 mL ethylene glycol in a 100 mL beaker under constant stirring. After the complete dissolution of $ZnCl_2$ in ethylene glycol, 5 mL of freshly prepared 1 M NaOH solution was added to the Zn(II) solution, and white colored solution was obtained. Then, to the white solution, 0.2 g of Se powder was added and kept under stirring for another 10 min. The as-obtained solution was transferred to a 50 mL Teflon-lined stainless steel autoclave and kept at 180 $^oC$ for 12 h. Finally, the reaction temperature was brought to room temepratture and washed 3 times with miliQ water and 2 times with ethanol to purify the material. The as-synthesized ZnSe powder was finally collected after drying at 60 $^oC$ for 2 h.

## Material Characterization

***Powder X-ray diffraction (PXRD).*** The phase purity and crystallinity of the synthesized material and the material after electrocatalysis were verified through powder X-ray diffraction using a BRUKER D8 Advance instrument fitted with a Cu-K$\alpha_1$ source ($\lambda$ = 1.5406 Å). The post-electrolysis powder sample was isolated from the electrode surface through sonication and was then studied using powder X-ray diffraction.

***Field emission scanning electron microscopy (FESEM).*** FESEM images of the synthesized materials and the materials deposited on nickel foam electrodes were captured using the TESCAN instrument (model Magna). The as-synthesized powder sample, was directly placed on a carbon tape for observation under the electron beam. Additionally, the electrodes after electrocatalysis were examined to assess the uniform deposition of the powder catalyst onto the nickel foam and to analyze their elemental composition. The TESCAN instrument was also used for STEM elemental mapping with an acceleration voltage of 30 kV. The sample for STEM was prepared on carbon coated TEM grid similar to that of TEM sample preparation.

***Transmission electron microscopy (TEM).*** TEM images of each sample were captured using a FEI Tecnai G2 20 S-TWIN transmission electron microscope (FEI Company, Eindhoven, Netherlands), featuring a $LaB_6$ electron source operating at an acceleration voltage of 200 kV. Carbon-coated 300 mesh grids from Ted Pella, USA, were used for the TEM study. For the post-catalytic TEM analysis, samples were extracted directly from the post-catalytic electrode surface under continuous sonication and subsequently transferred onto copper grids for further examination.

***X-ray photoelectron spectroscopy (XPS).*** The surface composition of both the as-prepared material and the material after electrocatalysis, along with subsequent elemental analysis, was directly analyzed through XPS. The measurements were carried out using the AXIS Supra instrument manufactured by Kratos Analytical Ltd., equipped with Al K$\alpha$ radiation as the X-ray source with hν = 1486.6 eV. Throughout the measurement process, the operational voltage and current were maintained at a constant level of 15 kV and 15 mA, respectively. The core-level XPS plot was deconvoluted using OriginLab 2020b software. The individual peak was fitted with PsdVoigt1 function using the multiple peak fit option.

***Brunauer–Emmett–Teller (BET) Analysis.*** The nitrogen adsorption-desorption and pore size distribution measurements were performed using the NOVA-2000e instrument, acquired from Quantachrome Instruments operated by the constant volume gas adsorption method. The nitrogen adsorption-desorption analysis was conducted at a constant temperature of 77 K. Before analysis, the sample was pre-treated by a gas-degassing method to cancel out any interference from adsorbed water or any other gases.

***Contact angle measurement.*** The contact angle measurements were performed using the KRUSS Drop Shape Analyser DSA100M system equipped with automatic syringes for customized liquid applications. For each contact angle measurement, water is used using the automatic syringe mode. All the results were analyzed using proprietary software provided with the system. The surface wettability test was performed on the thin pellets prepared with the powder samples.

***Raman spectroscopy.*** Raman measurements were conducted either directly on the powder samples, ex situ or under quasi-in-situ conditions directly on the electrode surface. A Raman microscope manufactured by HORIBA Scientific was utilized, featuring 532 nm and 785 nm lasers. The objective of the optical microscope was consistently set at 10x for each experiment, and all spectra were calibrated using standard crystalline Si spectra.

***Analyses of crystallographic parameters and assignment of valence State.*** Experimentally obtained powder X-ray diffraction patterns of $Fe_3X_4$ (X=Se, S, O) samples were correlated to the standard ICDD data. The crystallographic information files (CIFs) were obtained from the open-access databases[2-4] and were analyzed by the VESTA software. In a unit cell, the tetrahedral ($T_d$) and octahedral ($O_h$) iron site locations and bond parameters were analyzed using VESTA software.[4-11] According to the literature reports and bond parameters the tetrahedral or octahedral sites were assigned to the $Fe^{III}$ and $Fe^{II}$ centres.[2-4]

***Preparation of working electrode.*** The nickel foam was cleaned initially with 1 M HCl, followed by sonicating it for 15 minutes in Milli-Q water and acetone, respectively. The working electrode was prepared by drop-casting the catalyst on the cleaned surface of nickel foam (NF). To make the catalyst ink, a mixture of 25 mg of the material, 800 µL of isopropyl alcohol, and 200 µL of Nafion 117 solution was sonicated for approximately 30 minutes. Subsequently, different amounts of catalyst ink were drop-casted on the 1 x 1 $cm^2$ geometric surface area of the nickel foam surface which was air-dried overnight. The mass loading of the catalyst was determined from the difference in weight of the blank nickel foam and sample loaded nickel foam. For the glassy carbon (GC) electrode, the sample was drop-casted similarly and the catalyst loading was calculated based on the volume of catalyst ink drop-cast on the electrode surface.

***Electrochemical study.*** The electrochemical study was carried out in a three-electrode setup using 1 M KOH as an electrolyte, Hg/HgO (1 M NaOH) as a reference electrode (RE), graphite rod as a counter electrode (CE), and catalyst-loaded GC/NF as the working electrode (WE). All the electrochemical studies were carried out using Gamry 1010E-29165 potentiostat, commanded through the Gamry Framework software package.

The cyclic voltammetry (CV) and linear sweep voltammetry (LSV) data were recorded between a fixed potential region as mentioned in the main text or respective figure captions. Polarization curves of LSV studies were plotted after 85% iR-correction, done by post-run iR-correction module provided with the Gamry Framework software package. The solution resistance ($R_s$) required for iR-correction was also directly obtained from the equivalent circuit fitting of the electrochemical impedance spectroscopy (EIS). All the potentials reported for LSV and CV are calibrated to the reversible hydrogen electrode (RHE) scale in 1 M KOH (pH = 13.65) using the following equation:

$E(\text{RHE}) = E(\text{Hg/HgO}) + 0.098\ \text{V} + (0.059 \times \text{pH})\ \text{V}$ ……Eqn. S1

$\eta$ (Overpotential, OER) = E (RHE) – 1.23 V ……Eqn. S2

***In situ Raman Study.*** In situ Raman studies were conducted using a customized Raman cell designed to accommodate a three-electrode system within a single chamber, allowing direct exposure of the working electrode to the Raman laser. After configuring the reference and counter electrodes alongside the working electrode, the cell setup was connected to a potentiostat. The electrolyte chamber was filled with 10 mL of 1 M KOH solution and topped with an open lid featuring a window for the laser beam. To prevent any potential contact with the electrolyte, the optical microscope's objective was set to 10X magnification. For the in situ measurements, a 785 nm laser was used. Under varying timeframes at a fixed potential of 1.47 V vs RHE, the working electrode was analyzed through Raman spectroscopy, with a 15-second acquisition time for each spectrum. The laser intensity was limited to 10% to avoid spectral saturation, employing a 1200T grating with a slit width of 100 and a hole width of 300. All spectra were collected using LabSpec 6 software and presented without baseline correction. Prior to each experimental run, the Raman spectrometer was calibrated against a single crystalline silicon wafer to ensure accuracy.

***Tafel analysis.*** The Tafel slope measurements from the as-obtained linear sweep voltammetric curves were further plotted as the overpotential ($\eta$) in the y-axis *vs.* logarithm of the modulus of current density (log $j$) in the x-axis and thus the *ca.* slope is found to be equivalent of Tafel slope. Further, the Tafel slope was calculated according to the Tafel equation,

$\eta = b\log j + a$ ……Eqn. S3

where $\eta$ is the overpotential (V), $j$ is the current density (mA cm$^{-2}$), and $b$ is the Tafel slope (mV dec$^{-1}$).

***Determination of double-layer capacitance ($C_{dl}$) and electrochemical surface area (ECSA).*** Double layer capacitance ($C_{dl}$) was measured by recording CV cycles of the different electrodes in the non-faradaic region varying scan rate from 10 mV s$^{-1}$ to 200 mV s$^{-1}$. The potential range for every experiment was fixed between -0.15 and -0.05 V vs Hg/HgO and the $C_{dl}$ of each sample was calculated from the linear fit of the difference between the anodic and cathodic current at a fixed potential of 0.85 V vs RHE. Now, from the $C_{dl}$ value, the ECSA was calculated using the equation ECSA = $C_{dl}/C_s$, where, $C_s$ is defined as the specific capacitance of the material per unit area and the specific capacitance ($C_s$) value of 1.7 mF cm$^{-2}$ was considered for ECSA calculation.[4]

***Electrochemical impedance spectroscopy (EIS).*** Electrochemical impedance spectroscopy was conducted with a fixed bias potential of 0.570 V vs. Hg/HgO across various samples deposited on the NF, generating Nyquist plots. The EIS data were obtained through a comprehensive amplitude scan of a sinusoidal wave within a fixed frequency range from 100 kHz to 1 mHz. Subsequently, all Nyquist plots were fitted using an equivalent R-C circuit model. The charge-transfer resistance ($R_{ct}$) was determined from the semicircle diameter observed in the Nyquist plots.

***Analysis of the gas evolved during electrolysis.*** After a chronoamperometric (CA) study at a constant potential, about 1 mL of the headspace gas from the gas-tight cell (total headspace: 18 mL) was directly injected into the Agilent 8860 GC system equipped with TCD detectors with Argon carrier gas. The carrier gas flow rate was kept at 5 mL $min^{-1}$ and the oven temperature was kept isothermal at 40 $^oC$. To quantify the evolved gas, the calibration curve for the hydrogen was made using standard hydrogen gas purchased from Sigma Gases, India. The calibration curve was made by injecting different volumes of standard gases and by plotting the concentration vs peak area obtained from the GC chromatograms. The data analysis was carried out completely on the OpenLab EZChrom software provided by Agilent Technologies. From the calibration curve, a linear equation was obtained to quantify the amount of $H_2$ in µmol gas present in 1 mL injected gas (from the overhead space of the cathodic chamber) from the peak area in the GC chromatogram.

***Faradaic Efficiency (FE) calculation for hydrogen evolution reaction (HER).*** The Faradaic efficiency of the evolved $H_2$ was calculated from the amount of total charge (C) passed through the solution over some time of 2 h. The faradaic efficiency for $H_2$ ($FE_{H2}$) was calculated using the following equation.

FE (%) = [n (moles of $H_2$ formed) x ($ne^-$) x (F) / (Q)] x 100

where F is Faraday's constant (96,500 C $mol^{-1}$), n is the moles of $H_2$ determined from the GC, $ne^-$ is the number of electrons i.e., 2 for HER, and Q is the total charge passed through the reaction solution during the CA at 2.5 V (cell potential).

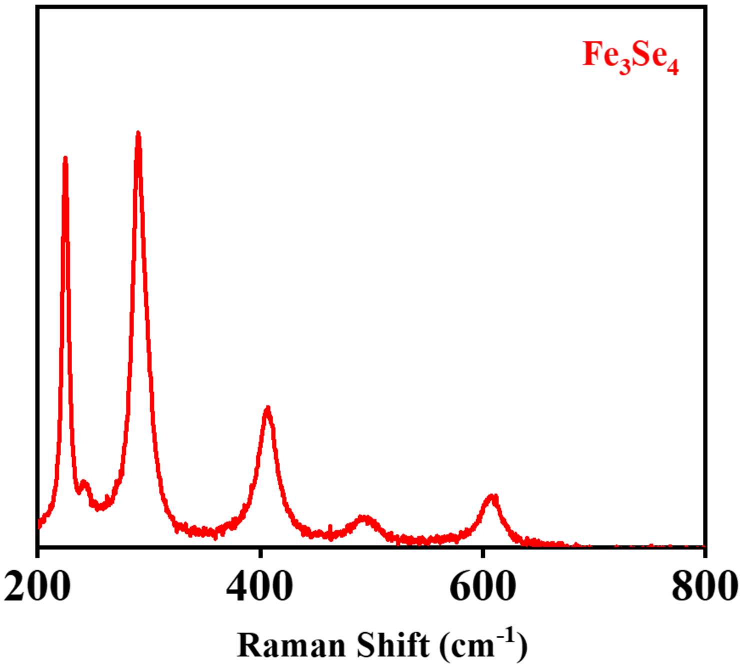

**Figure S1.** Raman spectra of the pristine $Fe_3Se_4$ powder sample.

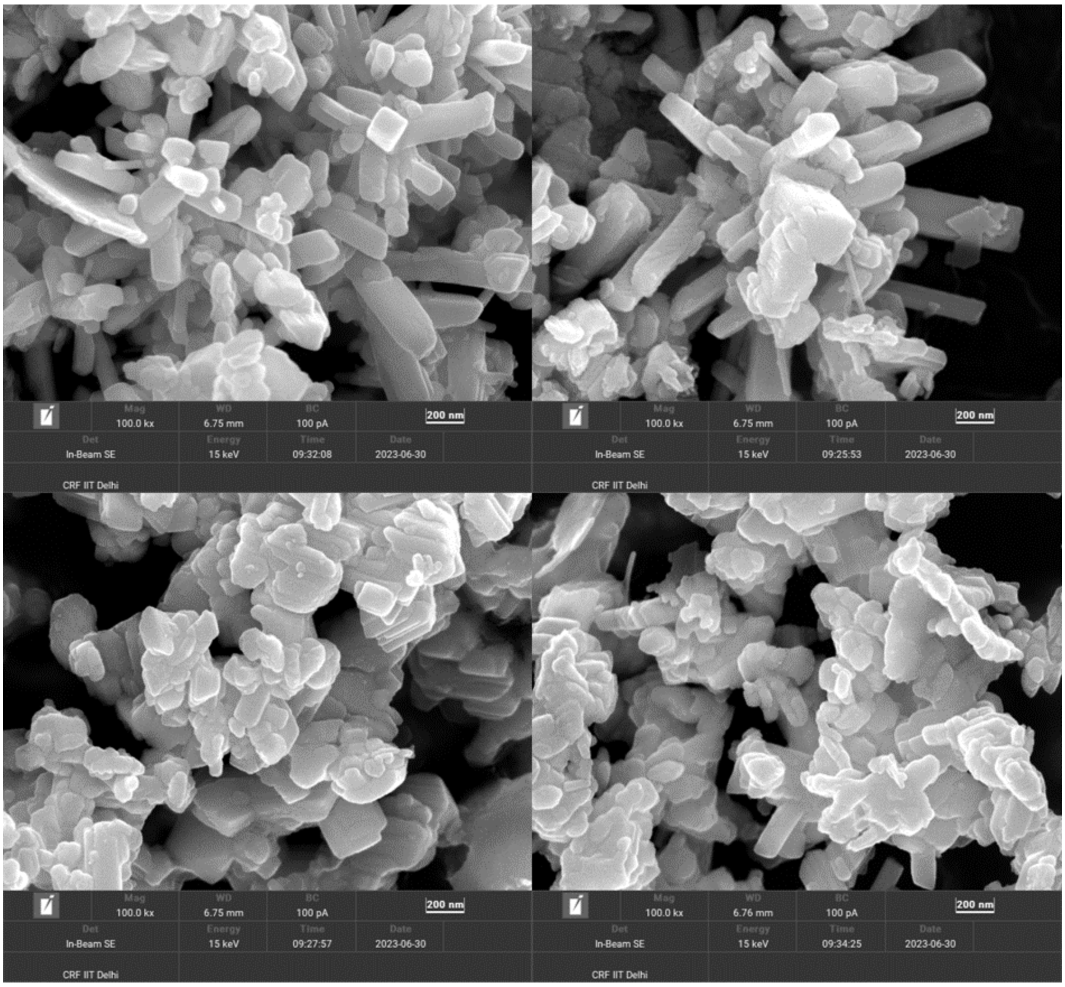

**Figure S2.** FESEM images of the pristine $Fe_3Se_4$ powder sample acquired at different magnifications.

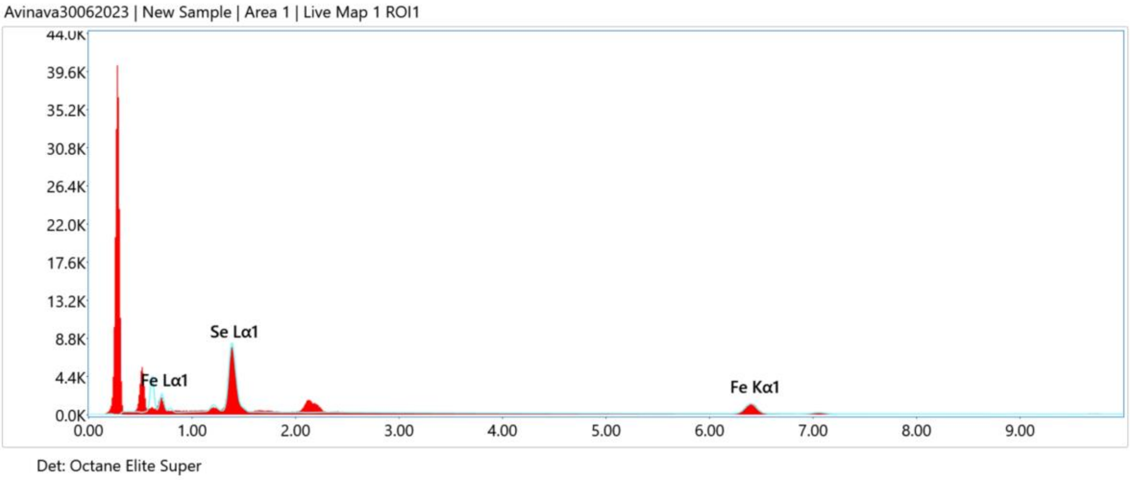

**Figure S3.** EDX spectrum of the pristine $Fe_3Se_4$ powder sample.

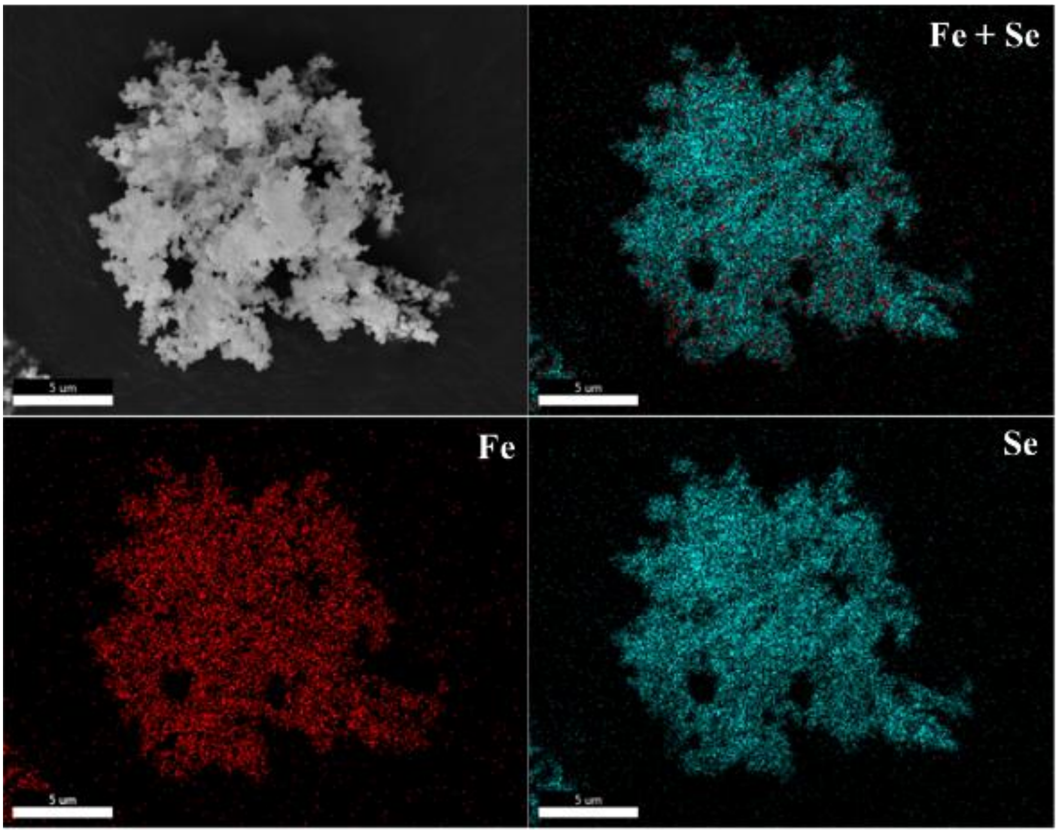

**Figure S4.** Elemental mapping of the pristine $Fe_3Se_4$ powder sample with uniform distribution of Fe and Se.

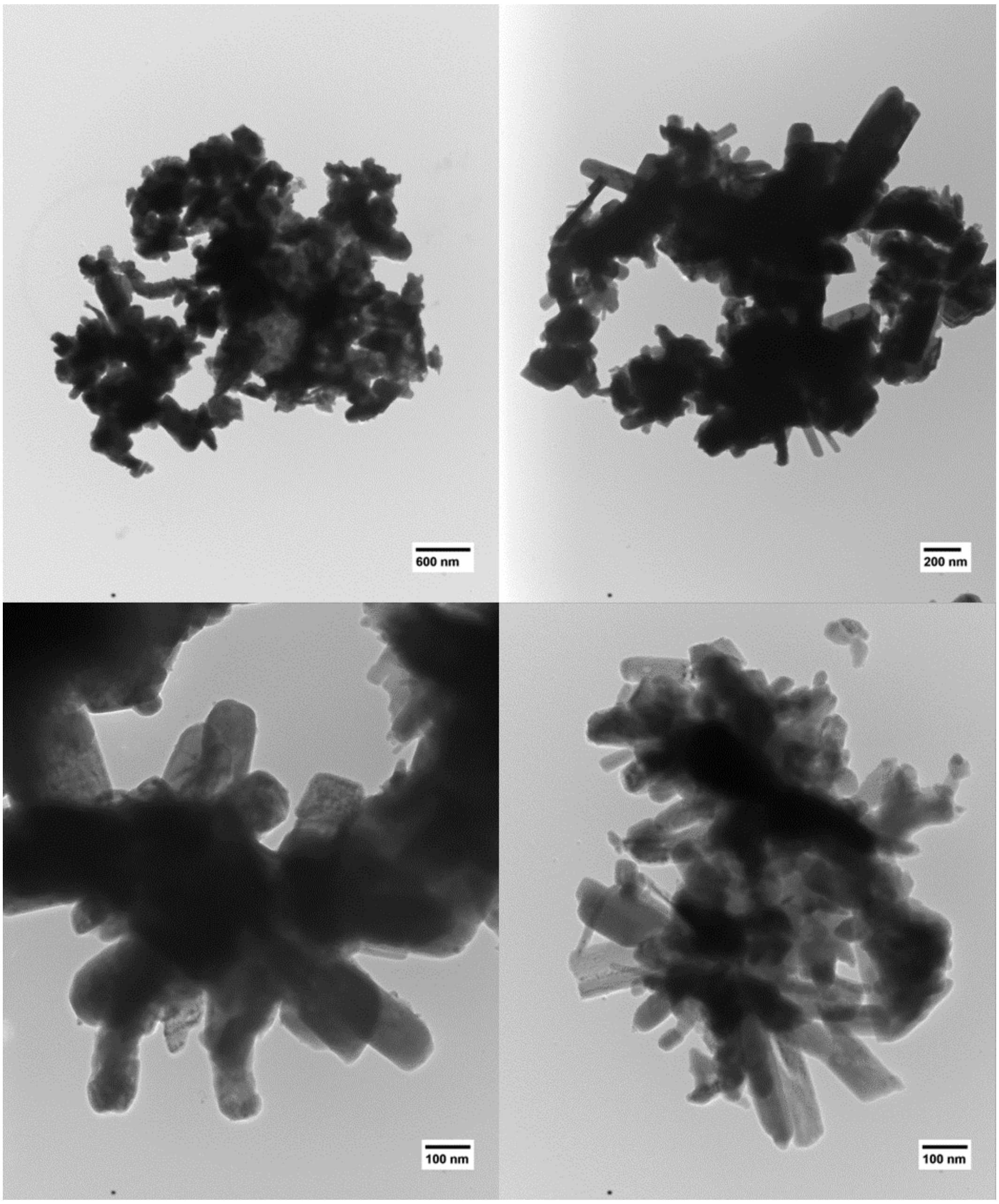

**Figure S5.** TEM images of the pristine $Fe_3Se_4$ powder sample acquired at different magnifications.

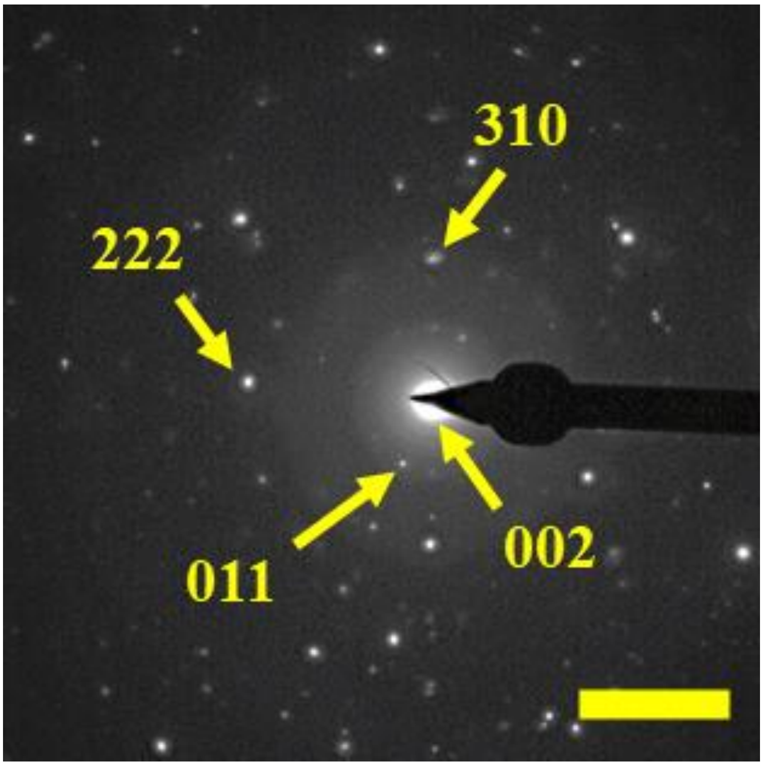

**Figure S6.** SAED pattern of the pristine $Fe_3Se_4$ powder sample (scale bar: 5 1/nm).

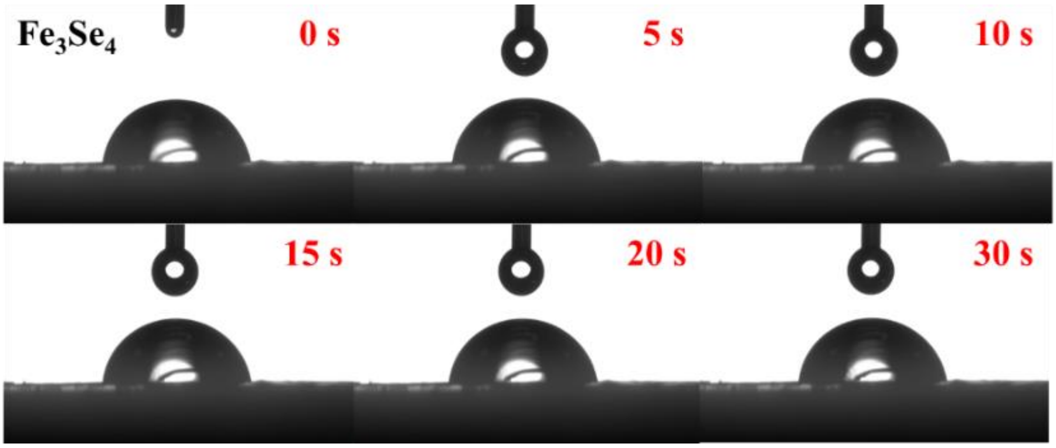

**Figure S7.** Time-dependent surface wettability test on the pristine $Fe_3Se_4$ sample.

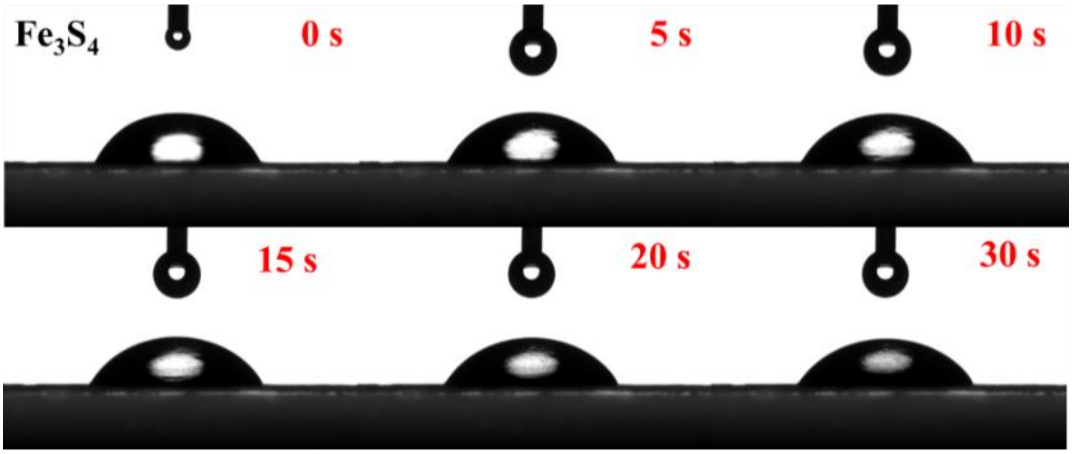

**Figure S8.** Time-dependent surface wettability test on the pristine $Fe_3S_4$ sample.

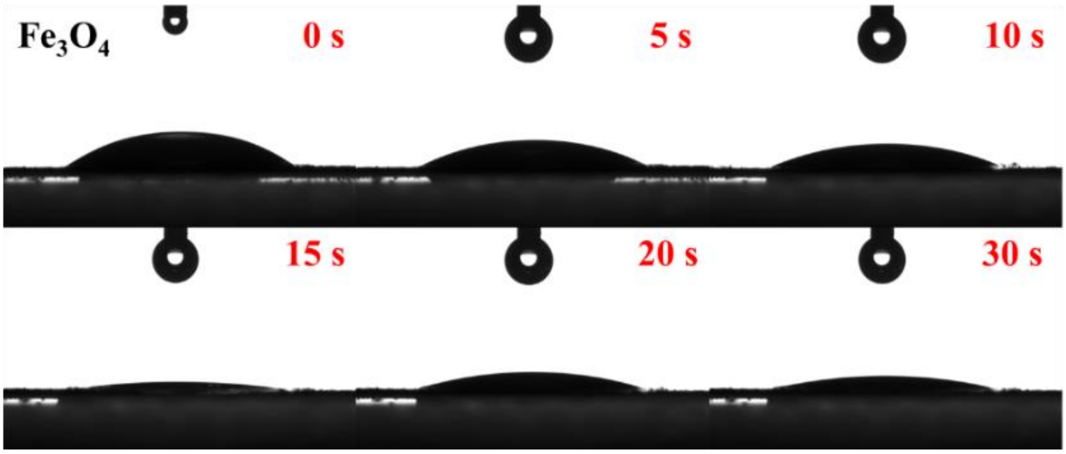

**Figure S9.** Time-dependent surface wettability test on the pristine $Fe_3O_4$ sample.

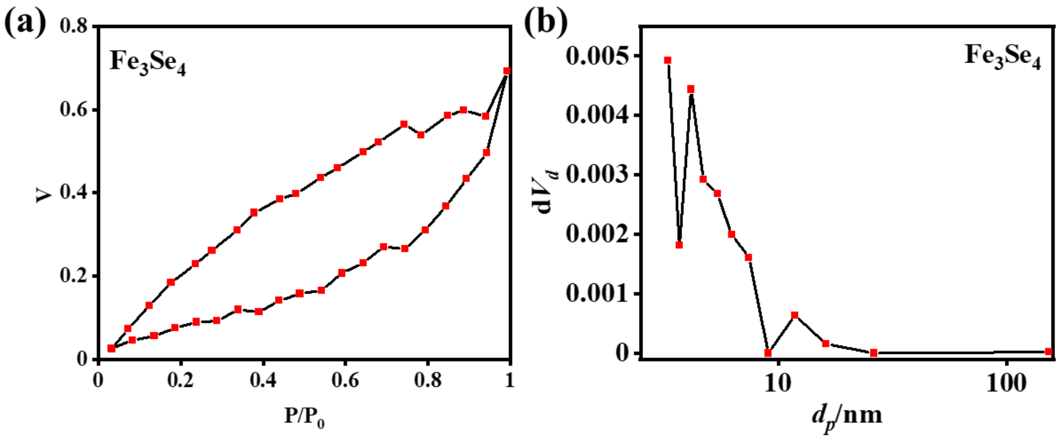

**Figure S10.** (a) $N_2$ adsorption-desorption isotherm recorded at 77 K and (b) pore-size distribution of powder $Fe_3Se_4$ sample.

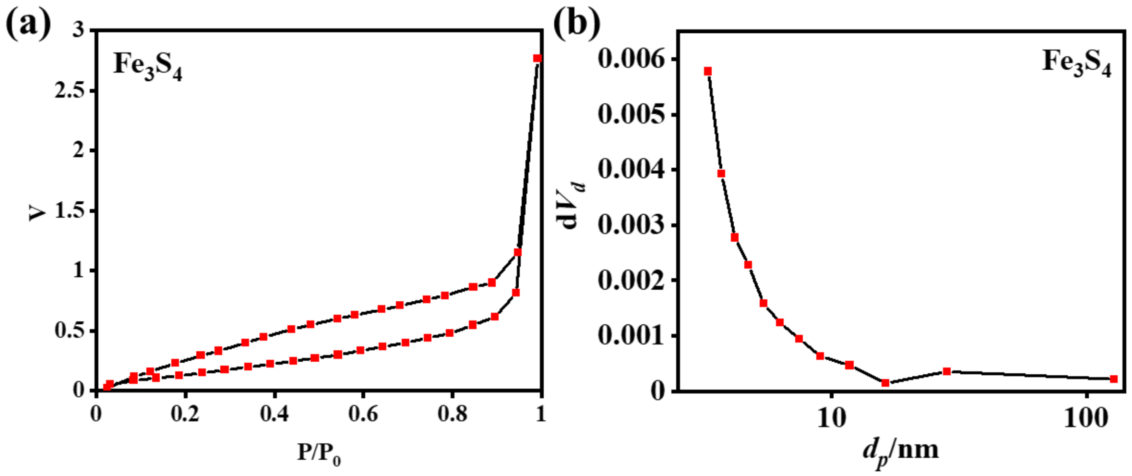

**Figure S11.** (a) $N_2$ adsorption-desorption isotherm recorded at 77 K and (b) pore-size distribution of powder $Fe_3S_4$ sample.

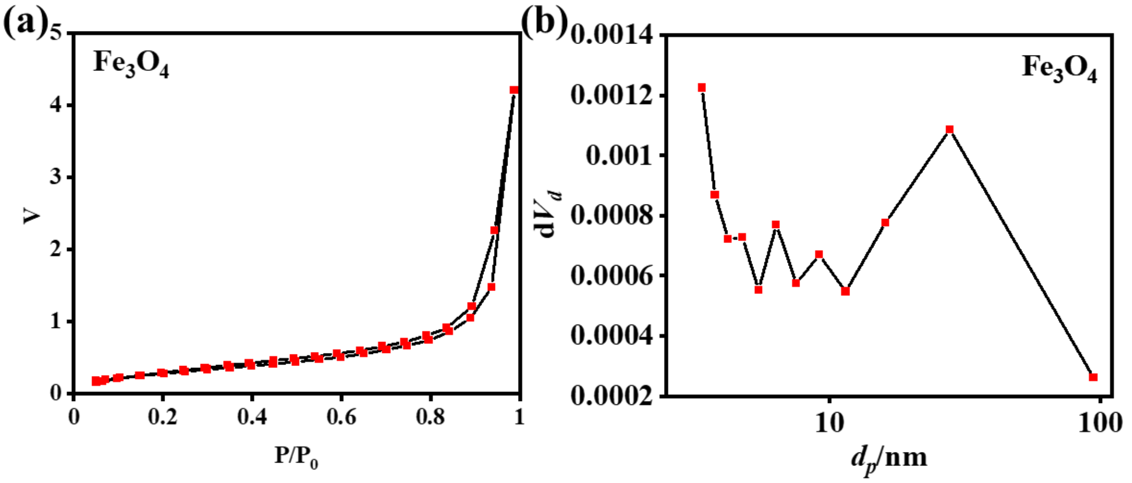

**Figure S12.** (a) $N_2$ adsorption-desorption isotherm recorded at 77 K and (b) pore-size distribution of powder $Fe_3O_4$ sample.

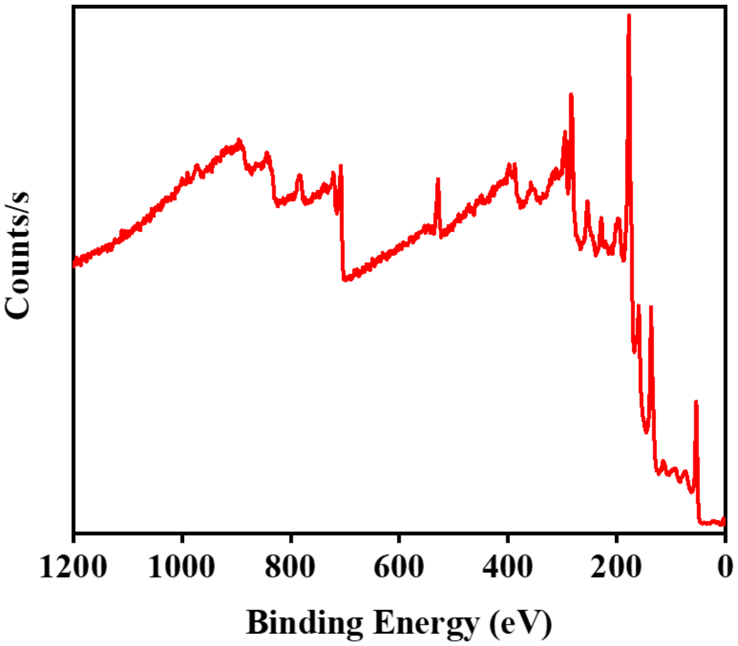

**Figure S13.** XPS survey scan of the as-synthesised powder $Fe_3Se_4$ sample.

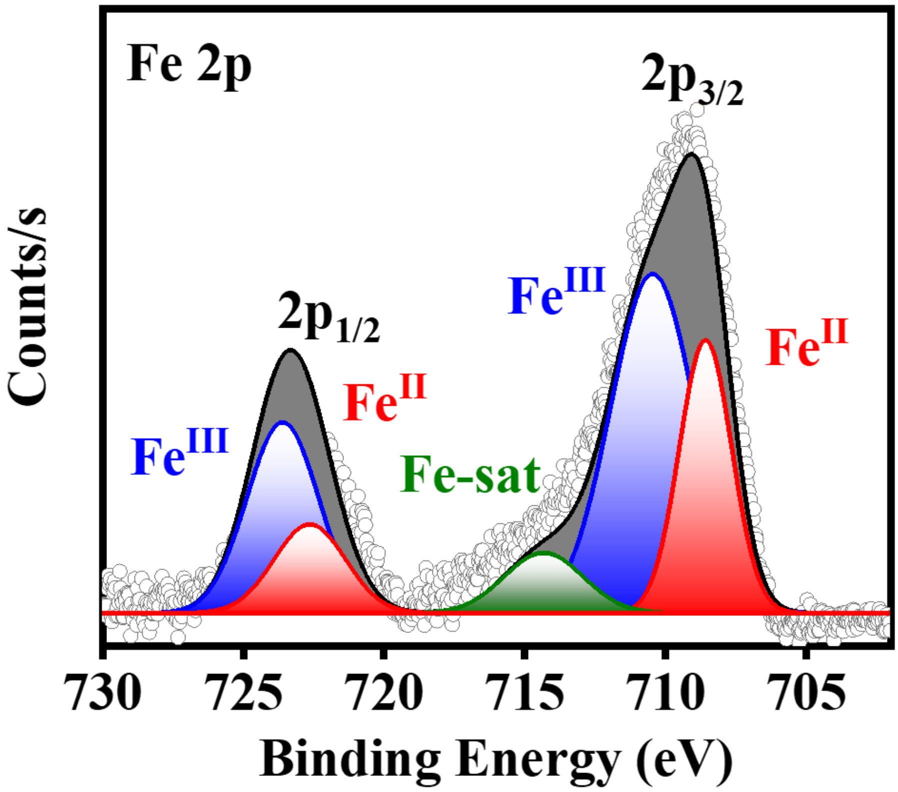

**Figure S14.** High-resolution Fe 2p XPS spectra of the pristine $Fe_3S_4$ powder sample.

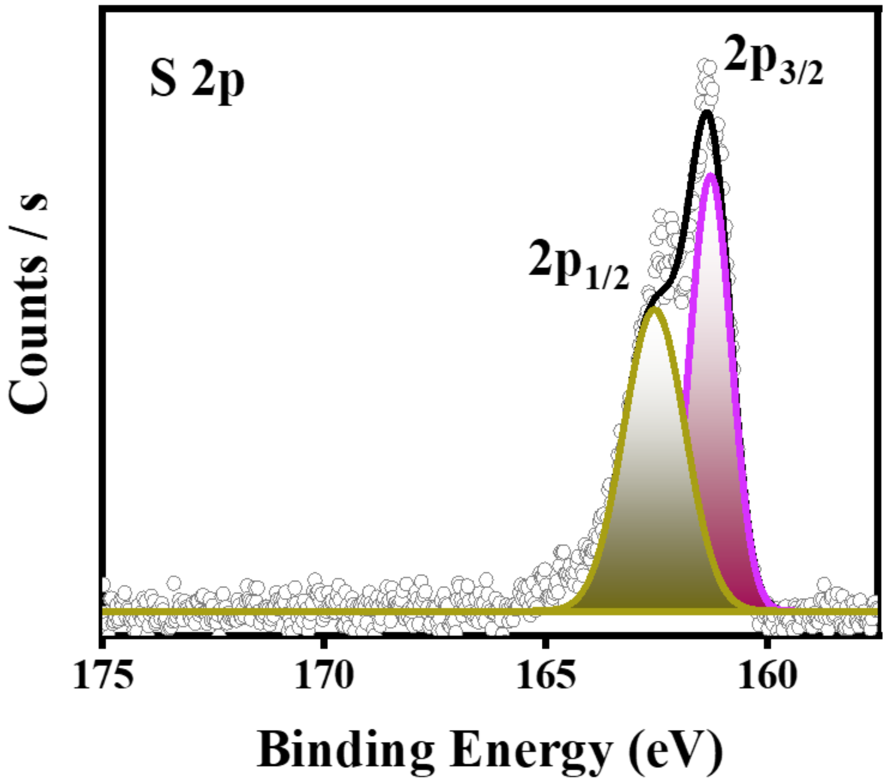

**Figure S15.** Core-level S 2p XPS spectra of the pristine $Fe_3S_4$ powder sample.

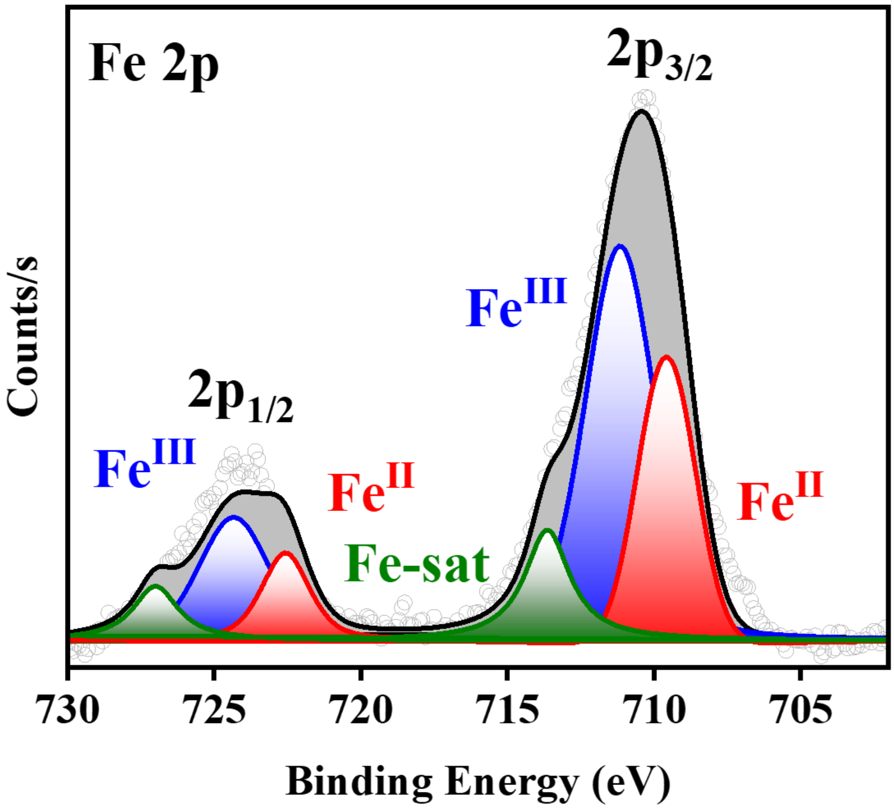

**Figure S16.** Core-level Fe 2p XPS spectra of the pristine $Fe_3O_4$ powder sample.

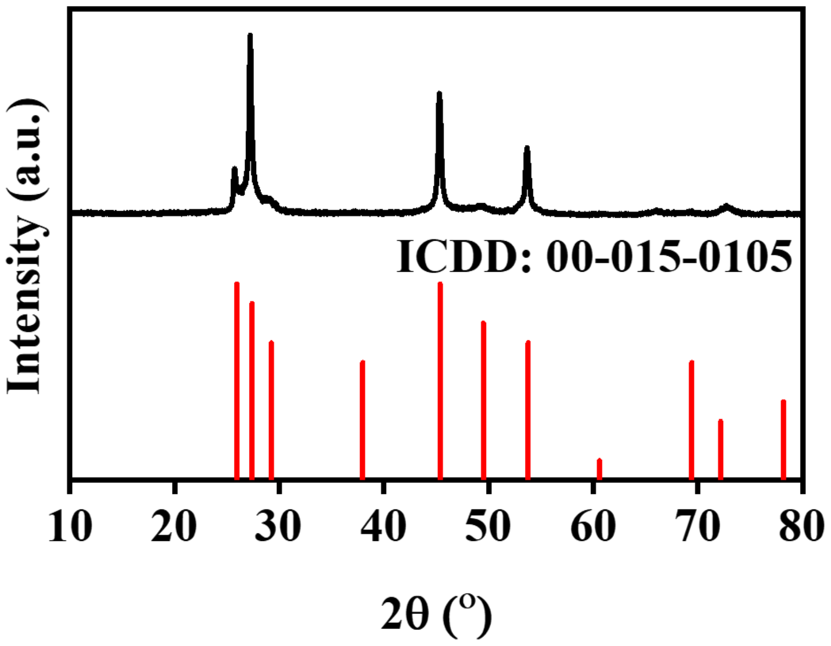

**Figure S17.** PXRD pattern of the as-synthesised ZnSe powder sample.

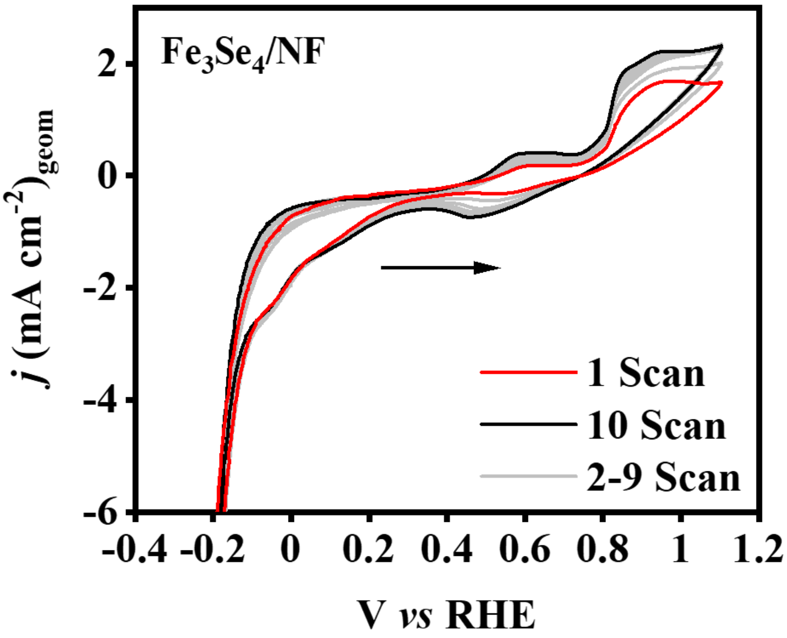

**Figure S18.** CV cycles recorded with the $Fe_3Se_4$/NF electrode within potential range -0.2 to 1.1 V vs RHE at a scan rate of 5 mV $s^{-1}$.

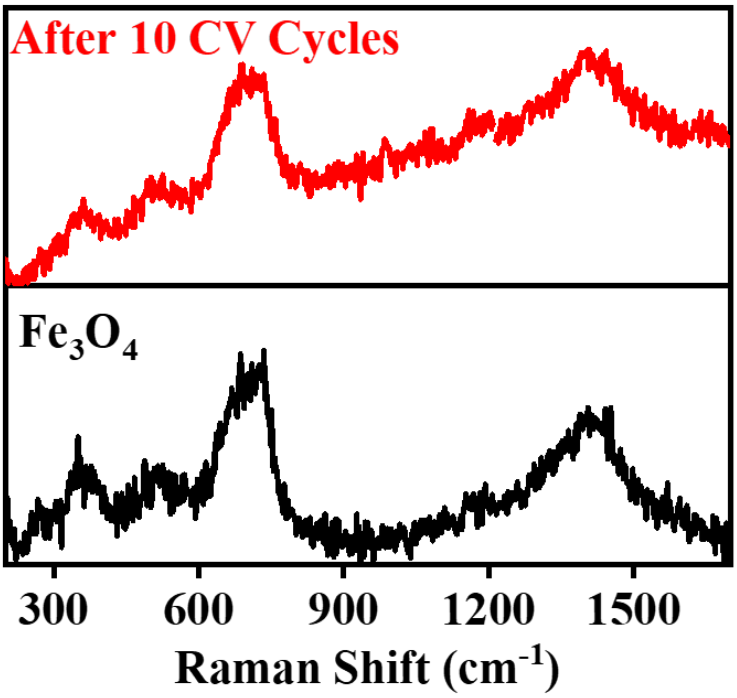

**Figure S19.** Raman spectra of the $Fe_3O_4$/NF electrode before (black) and after (red) 10 CV cycles at scan rate 5 mV s$^{-1}$.

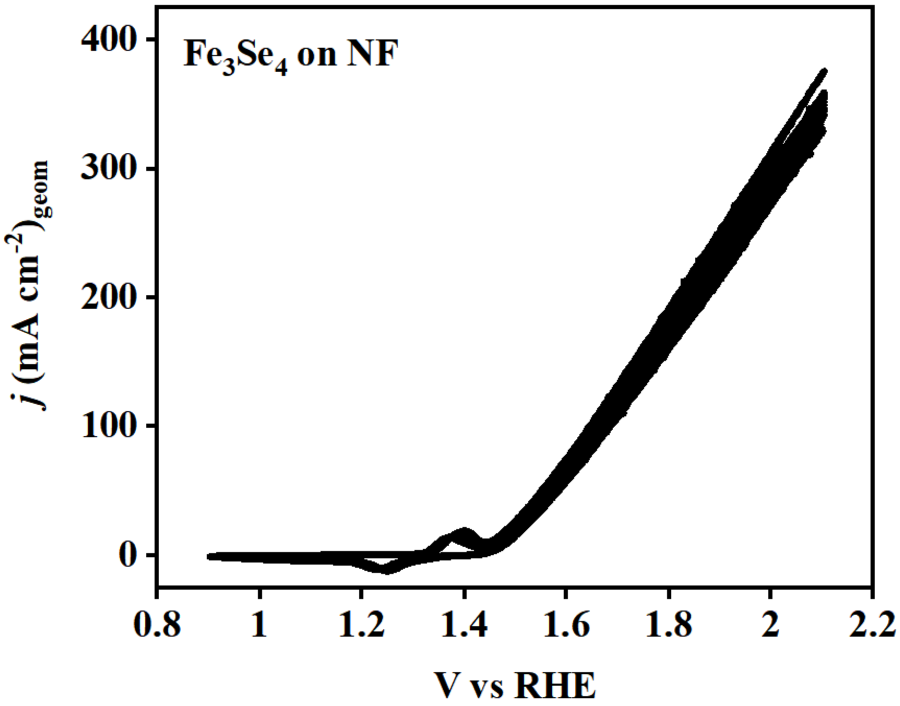

**Figure S20.** CV cycles performed in 1 M KOH at 1 mV s$^{-1}$ for the pristine $Fe_3Se_4$ powder sample drop casted on NF.

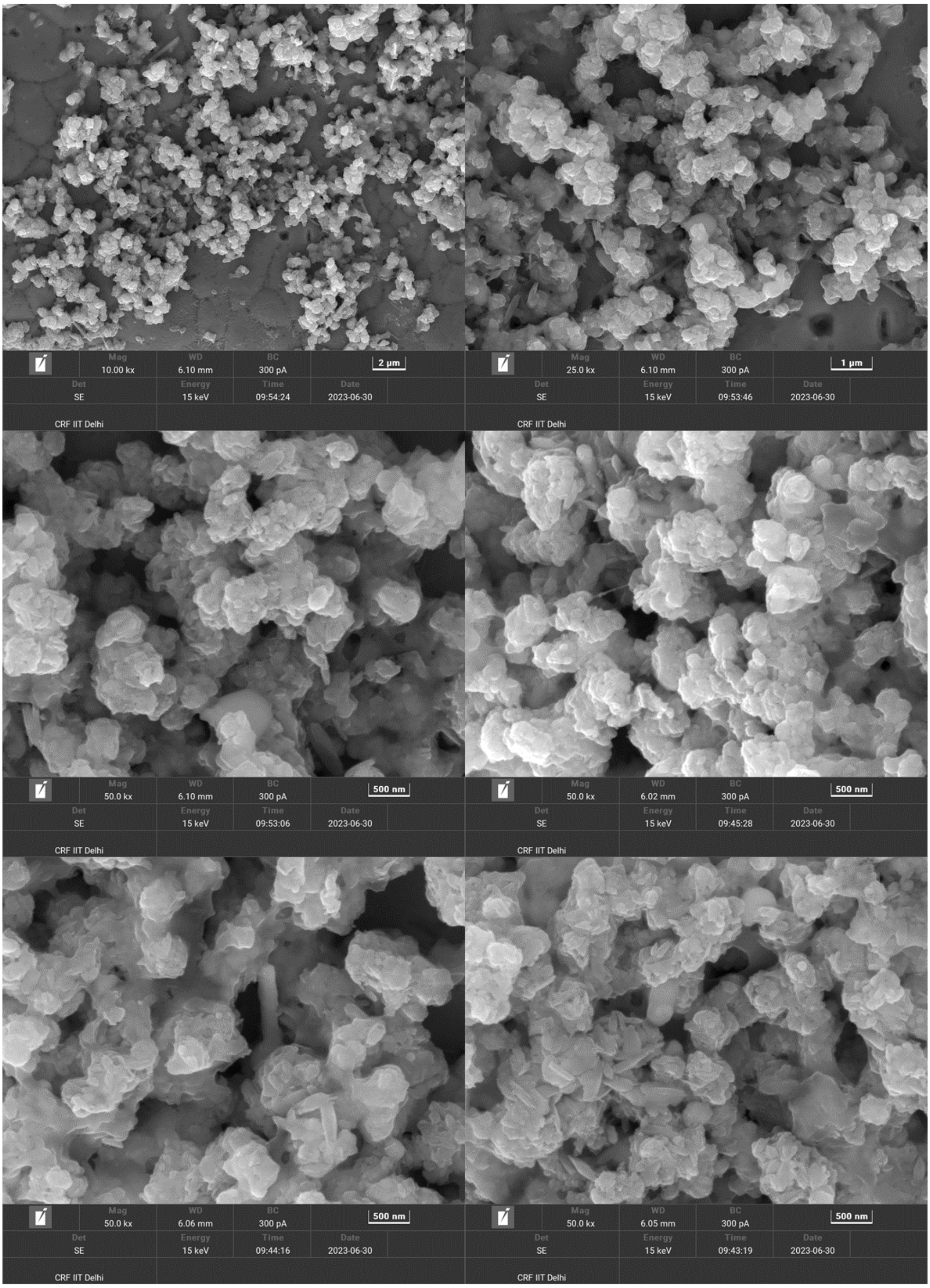

**Figure S21.** FESEM images collected on the $Fe_3Se_4$/NF electrode surface after 12 h CA study at 1.47 V vs RHE.

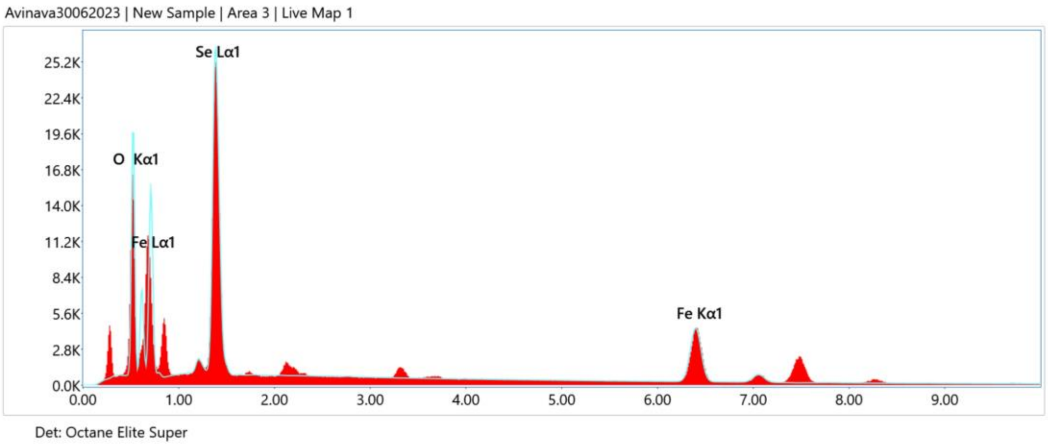

**Figure S22.** EDX spectrum obtained from the $Fe_3Se_4$/NF electrode surface after 12 h CA study at 1.47 V vs RHE.

**Table S1.** The ICP-MS study report of the post-CA electrolyte.

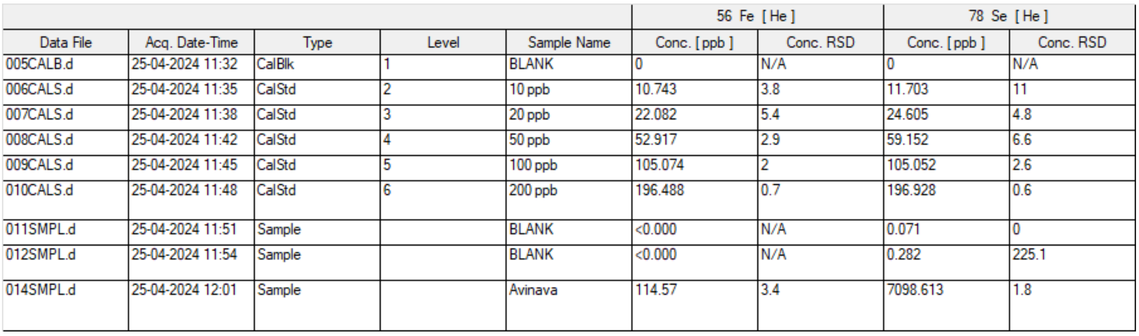

| | | | | | 56 Fe [ He ] | | 78 Se [ He ] | |
|---|---|---|---|---|---|---|---|---|
| Data File | Acq. Date-Time | Type | Level | Sample Name | Conc. [ ppb ] | Conc. RSD | Conc. [ ppb ] | Conc. RSD |
| 005CALB.d | 25-04-2024 11:32 | CalBlk | 1 | BLANK | 0 | N/A | 0 | N/A |
| 006CALS.d | 25-04-2024 11:35 | CalStd | 2 | 10 ppb | 10.743 | 3.8 | 11.703 | 11 |
| 007CALS.d | 25-04-2024 11:38 | CalStd | 3 | 20 ppb | 22.082 | 5.4 | 24.605 | 4.8 |
| 008CALS.d | 25-04-2024 11:42 | CalStd | 4 | 50 ppb | 52.917 | 2.9 | 59.152 | 6.6 |
| 009CALS.d | 25-04-2024 11:45 | CalStd | 5 | 100 ppb | 105.074 | 2 | 105.052 | 2.6 |
| 010CALS.d | 25-04-2024 11:48 | CalStd | 6 | 200 ppb | 196.488 | 0.7 | 196.928 | 0.6 |
| 011SMPL.d | 25-04-2024 11:51 | Sample | | BLANK | <0.000 | N/A | 0.071 | 0 |
| 012SMPL.d | 25-04-2024 11:54 | Sample | | BLANK | <0.000 | N/A | 0.282 | 225.1 |
| 014SMPL.d | 25-04-2024 12:01 | Sample | | Avinava | 114.57 | 3.4 | 7098.613 | 1.8 |

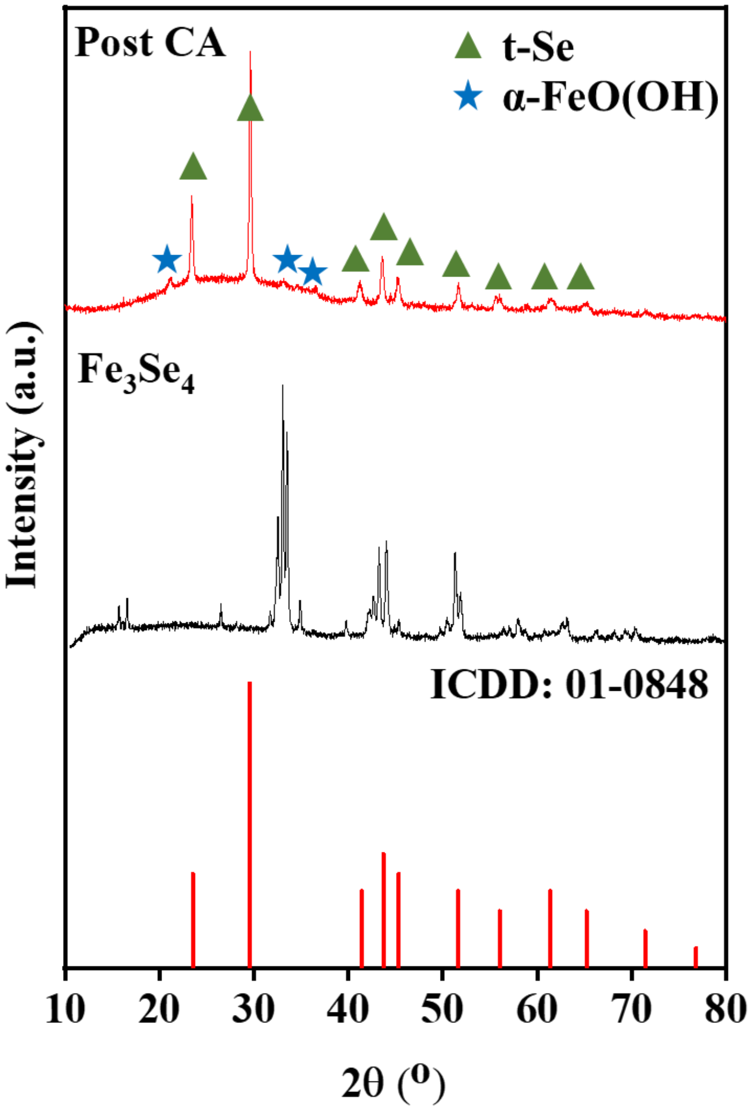

**Figure S23.** Post-CA PXRD pattern identify the presence of both α-FeO(OH) and t-Se. Bottom: bar plot for standard t-Se reported in ICDD card 01-0848.

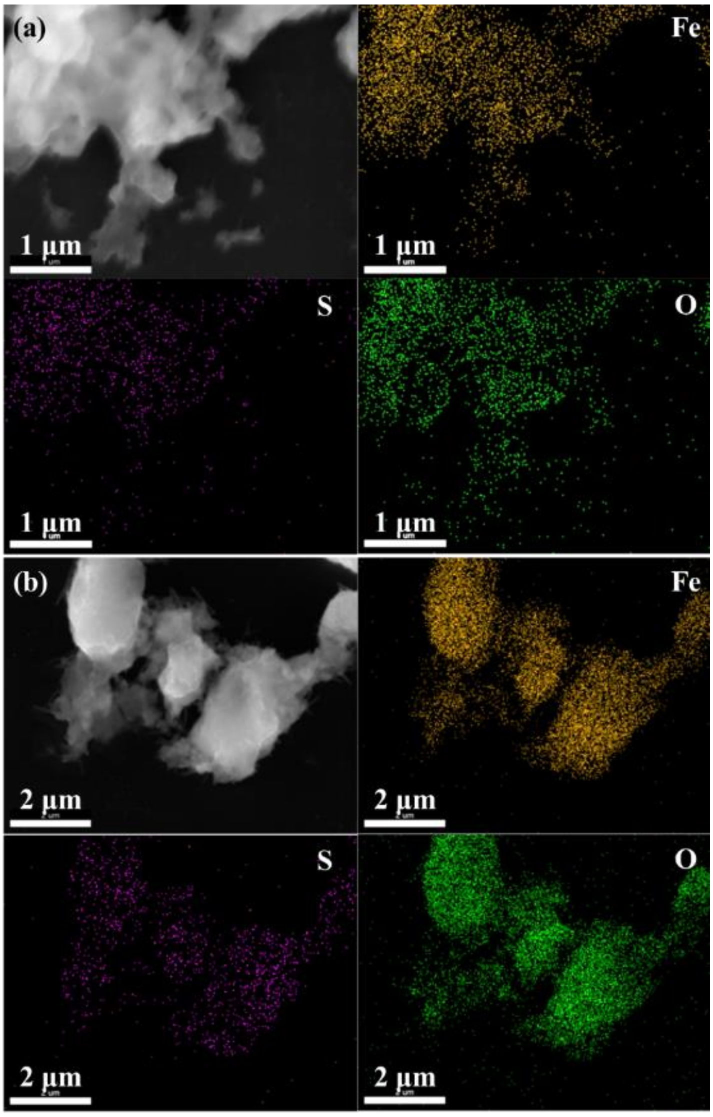

**Figure S24.** Post-CA elemental mapping in STEM mode identifying uniform distribution of Fe and O, with discrete presence of S.

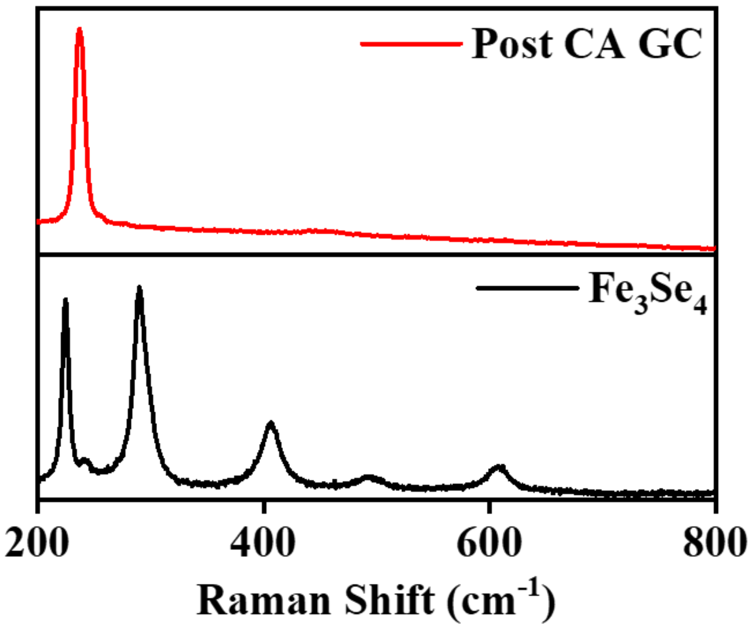

**Figure S25.** The post-CA Raman spectra recorded from the isolated powder sample from the glassy carbon (GC) electrode after 12 h chronoamperometry at 1.5 V vs RHE.

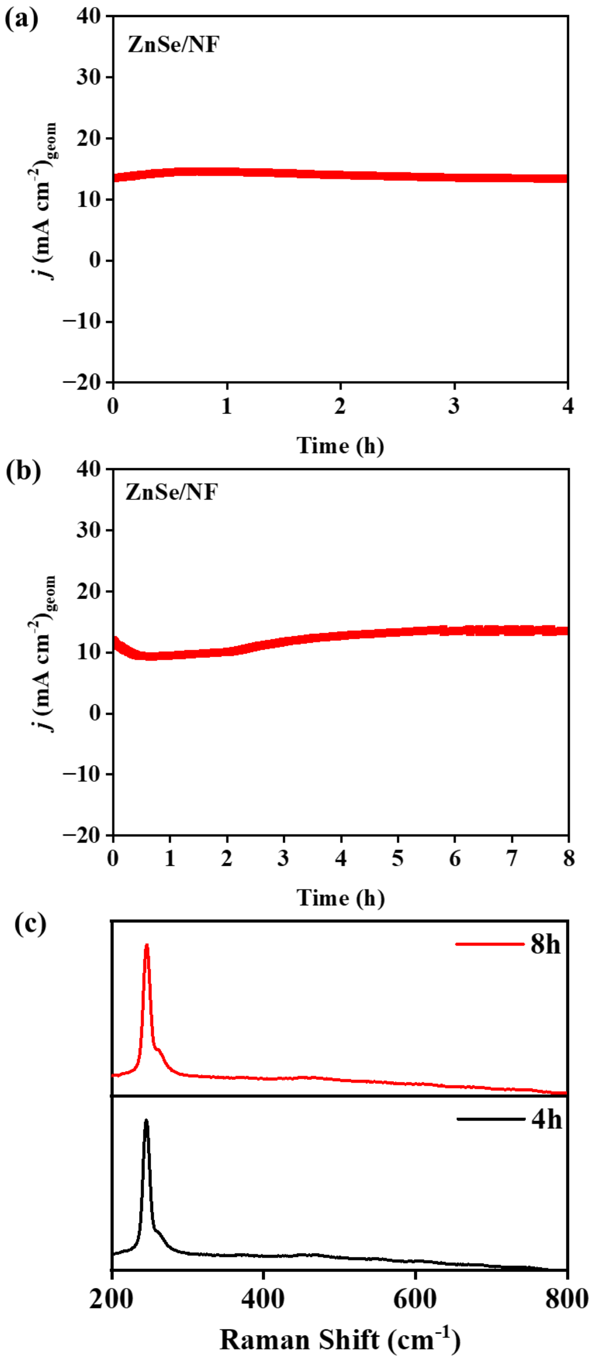

**Figure S26.** Chronoamperometric study of the ZnSe/NF electrode for (a) 4 h and (b) 8 h at 1.52 V vs RHE and (c) Raman spectra directly observed on the electrode surface after 4 h and 8 h CA.

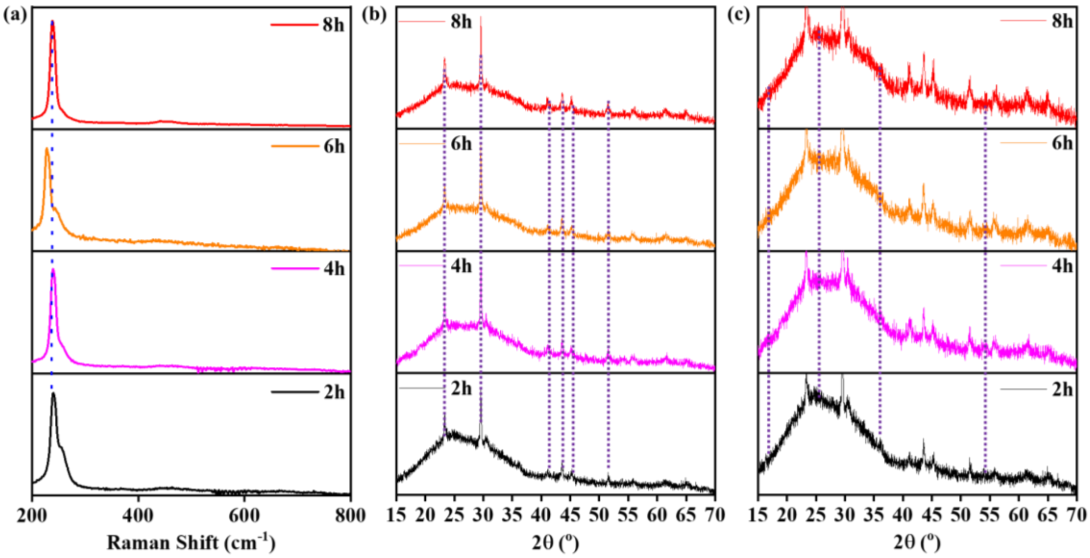

**Figure S27.** (a) Raman spectra and (b) PXRD data recorded at different time interval at an applied potential of 1.47 vs RHE. (c) Magnified version of the panel b (PXRD).

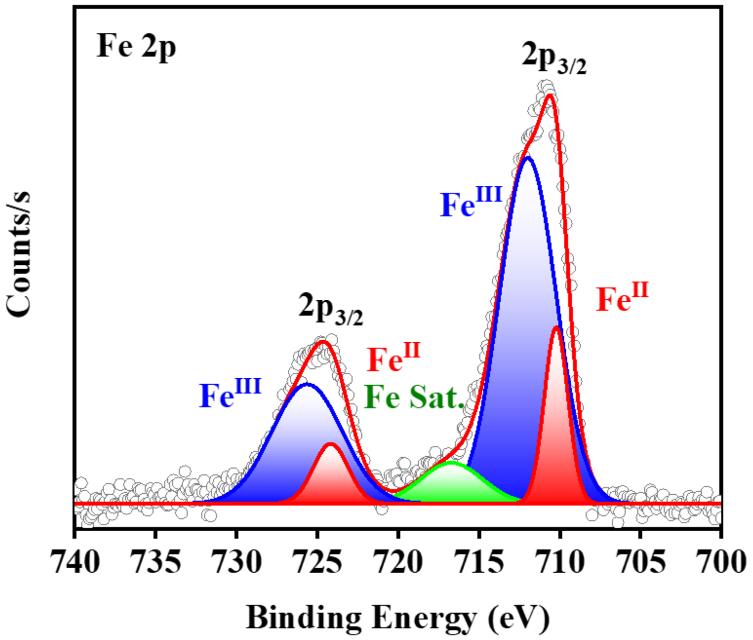

**Figure S28.** Core-level Fe 2p XP spectrum obtained from the $Fe_3Se_4$/NF electrode surface after 12 h CA study at 1.47 V vs RHE.

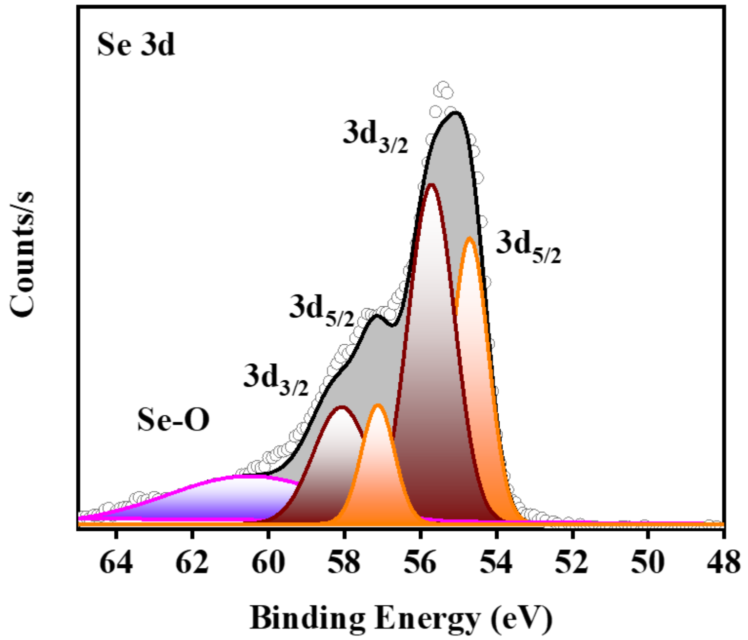

**Figure S29.** Core-level Se 3d XP spectrum obtained from the $Fe_3Se_4$/NF electrode surface after 12 h CA study at 1.47 V vs RHE.

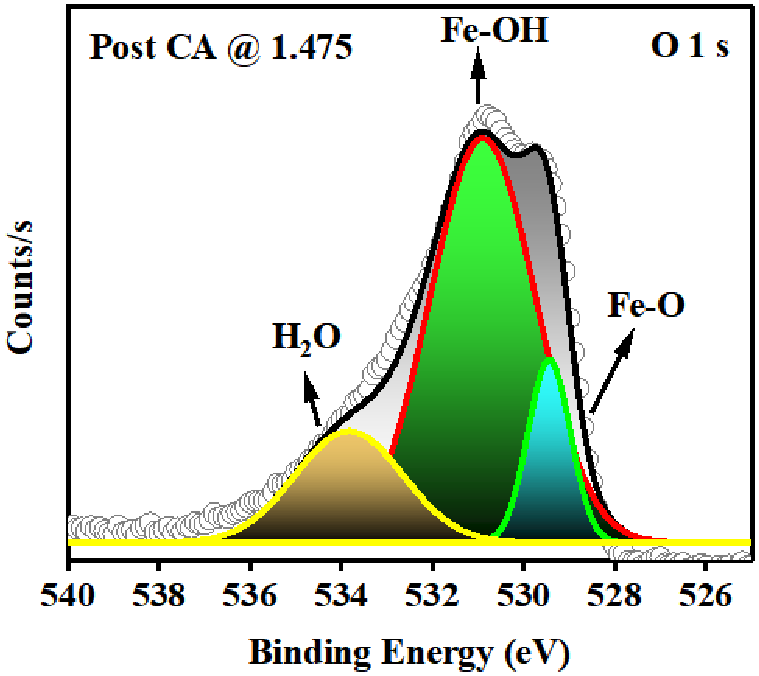

**Figure S30.** Core-level O 1s XP spectrum obtained from the $Fe_3Se_4$/NF electrode surface after 12 h CA study at 1.47 V vs RHE.

**Table S2.** OER activity of α-FeO(OH)/t-Se and some reported Fe-based electrocatalysts .

| **Catalysts** | **Substrate** | **$\eta$(mV)** | **b (mV dec$^{-1}$)** | **Stability (h)** | **Ref.** |
|---|---|---|---|---|---|
| **α-FeO(OH)/t-Se** | NF[a] | 219 | 49 | 10 (CA @ 1.47 V) | **This Work** |
| **$FeSe_2$ nanoplates** | NF[a] | 330 | 48.1 | 70 (CA @ 1.67 V) | [12] |
| **$FeSe_2$** | NF[a] | 245 |  | 18 (CP @ 10 mA) | [13] |
| **$Fe_3S_4$** | NF[a] | 251 | 45.9 | 12 (CA @ 1.59 V) | [1] |
| **$Fe_3S_4$** | CFP[b] | 230 | 50 | 17 (CA) | [14] |
| **$Fe_3S_4$-$Fe_7Se_8$@C** | NF[a] | 219 | 45.4 | 12 (CA @ 1.46 V) | [15] |
| **$Fe_7S_8$** | GC[c] | 270 | 43 | 24 (CP @ 10 mA) | [16] |
| **FeS** | IF[d] | 238 | - | 30 (CA) | [17] |
| **FeS** | IF[d] | 537 ($j$=100) | - | - | [17] |
| **$FeS_2$** | GC[c] | 450 | 151 | - | [18] |
| **$FeS_2$** | NF[a] | 189 | 71 | 5 (CA) | [19] |
| **$FeS_2$** | NF[a] | 250 | - | 5 (CP) | [20] |
| **FeB** | GC[c] | 296 | 52.4 | - | [21] |
| **Fe–B–O@$Fe_2B$** | NiF[e] | 273 | 58.7 | - | [22] |
| **Fe–B–O@$FeB_2$** | NiF[e] | 260 | 57.9 | - | [22] |
| **FeP nanorods** | CP[f] | 350 | 63.6 | 48 (CP) | [23] |
| **FeOOH** | NF[a] | 428 | 44 | 10 (CA @ 1.52 V) | [24] |
| **FeOOH** | GC[c] | 530 | 67 | - | [25] |
| **FeOOH** | NF[a] | 290 | 48 | 11 (CA @ 1.52 V) | [26] |
| **FeOOH nanosheet** | NF[a] | 390 | 78.6 | 24 (CP @ 10 mA) | [27] |
| **FeOOH** | NF[a] | 280 | 47 | 48 (CA @ 1.53 V) | [28] |
| **FeNiP** | NF[a] | 180 | 76 | 24 (CP @ 10 mA) | [29] |
| **$Fe_3W_1$** | Au[g] | 410 | 51.7 | 12 (CA) | [30] |
| **FeSi** | NF[a] | 219 | 39 | 24 (CP @ 10 mA) | [31] |
| **$NiFeO_x$** | GC[c] | 350 | - | 2 (CP @ 10 mA) | [32] |
| **FeNi@NGE** | NF[a] | 275 | 41.2 | 12 (CA) | [33] |
| **NiFe** | NF[a] | 215 | 28 | 10 (CP @ 25 mA) | [34] |
| **$FeSn_2$** | NF[a] | 197 | - | 24 (CA @ 1.53 V) | [35] |
| **FeCo-$Co_4N$** | N-C | 280 | 40 | 12 (CA) | [36] |
| **$FeCoWO_x$** | AF[h] | 191 | - | 550 (CP @ 30 mA) | [37] |

[a]Nickel Foam, [b]carbon fibre paper, [c]glassy carbon electrode, [d]iron foam, [e]nickel foil, [f]carbon paper, [g]gold electrode, [h]gold foam

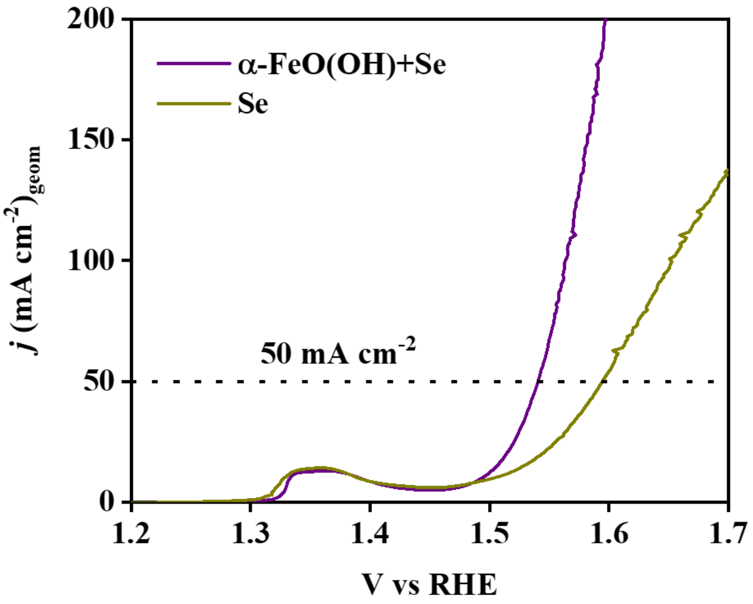

**Figure S31.** Polarization curves obtained with a mixture of α-FeO(OH) + Se (1:1 in wt%) and commercial Se powder as control experiments.

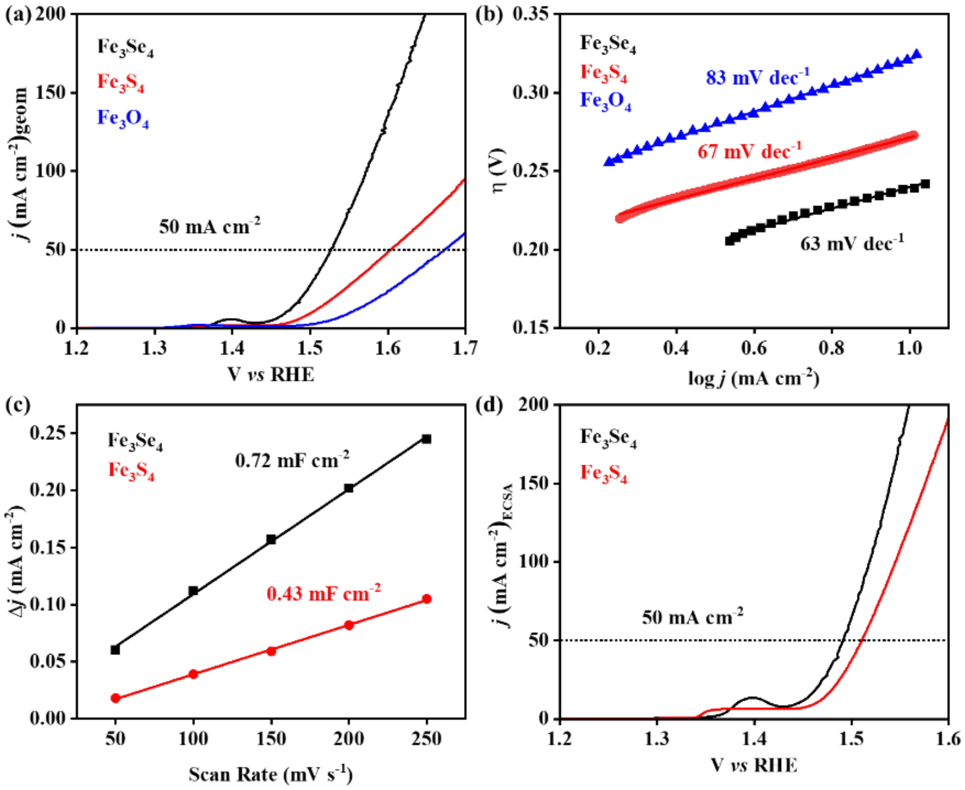

**Figure S32.** (a) LSV Polarization curves, (b) Tafel plot, (c) Double-layer capacitance ($C_{dl}$) obtained with pristine $Fe_3Se_4$/NF, $Fe_3S_4$/NF and $Fe_3O_4$/NF anode. (d) ECSA normalized LSV plots obtained for $Fe_3Se_4$/NF and $Fe_3S_4$/NF anode.

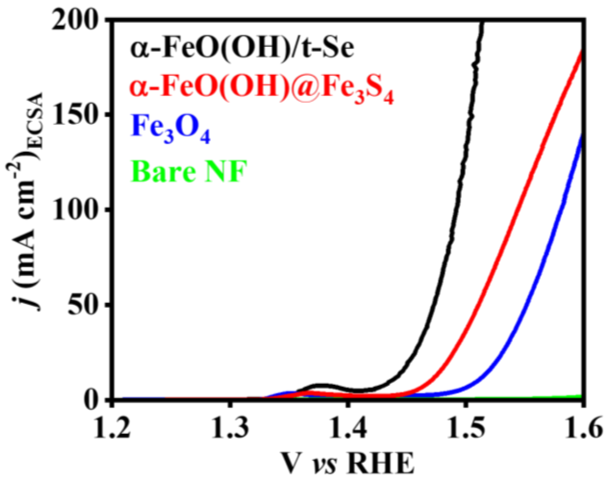

**Figure S33.** ECSA normalized polarization curves recorded in between 1.2 to 1.6 V vs RHE for α-FeO(OH)/t-se, α-FeO(OH)@Fe$_3$S$_4$, Fe$_3$O$_4$ and bare NF electrodes.

**Table S3.** The electrochemical activity parameters for the pristine Fe$_3$X$_4$/NF electrode and electro-modified catalyst after CA/CV activation.

| **Catalysts** | **η (mV) @10mA cm$^{-2}$** | **b (mV dec$^{-1}$)** | **C$_{dl}$ (mF cm$^{-2}$)** | **ECSA (cm$^2$)** |
|---|---|---|---|---|
| **α-FeO(OH)/t-Se** | 219 | 49 | 1.18 | 0.70 |
| **Fe$_3$Se$_4$** | 254 | 63 | 0.72 | 0.43 |
| **α-FeO(OH)/Fe$_3$S$_4$** | 251 | 45.9 | 1.14 | 0.67 |
| **Fe$_3$S$_4$** | 300 | 67 | 0.43 | 0.25 |
| **Fe$_3$O$_4$** | 321 | 61 | 0.68 | 0.40 |

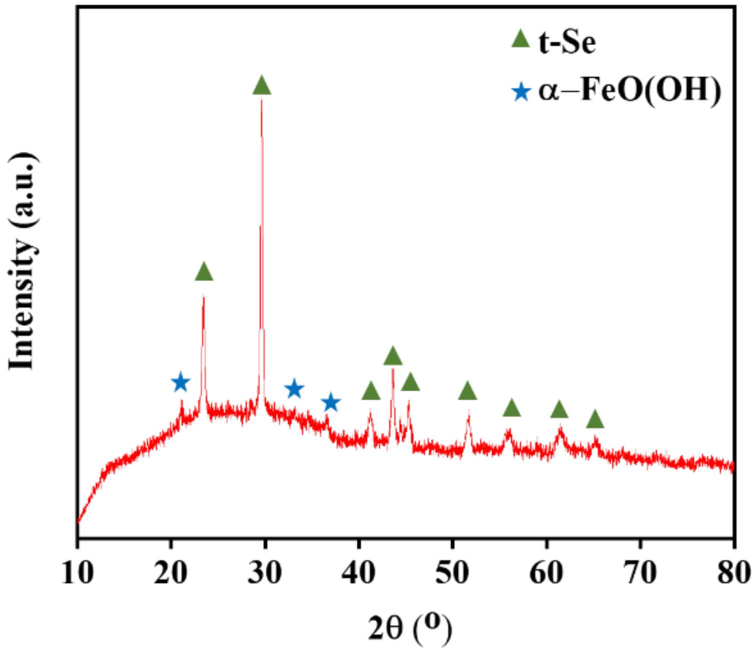

**Figure S34:** PXRD pattern of the α-FeO(OH)/t-Se electrode after 10 h OER CA at 1.5 V vs RHE.

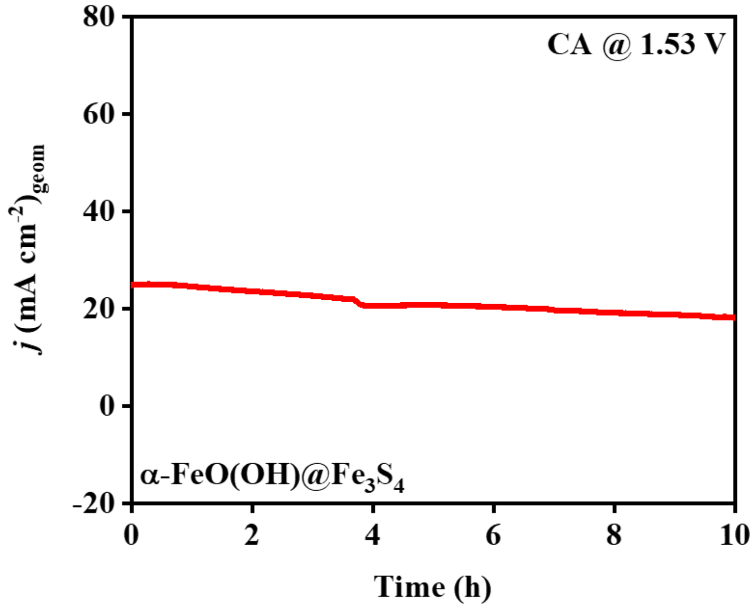

**Figure S35:** OER CA study for 10 h of the α-FeO(OH)@$Fe_3S_4$ electrode at 1.53 V vs RHE.

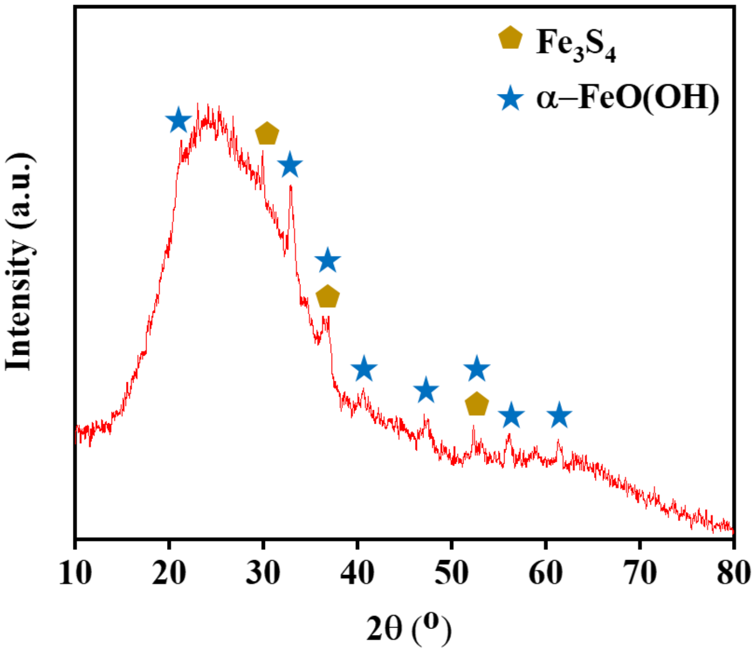

**Figure S36:** PXRD pattern of the α-FeO(OH)@$Fe_3S_4$ electrode after 10 h OER CA at 1.53 V vs RHE.

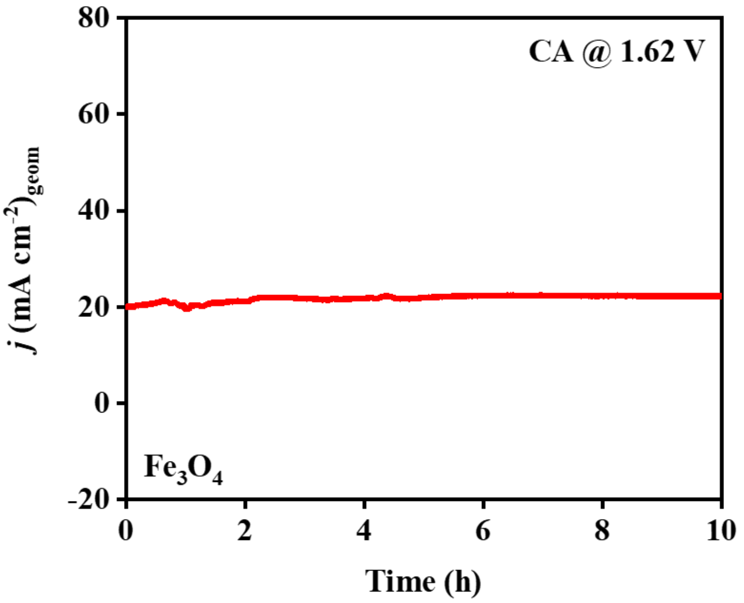

**Figure S37:** OER CA study for 10 h of the $Fe_3O_4$ electrode at 1.62 V vs RHE.

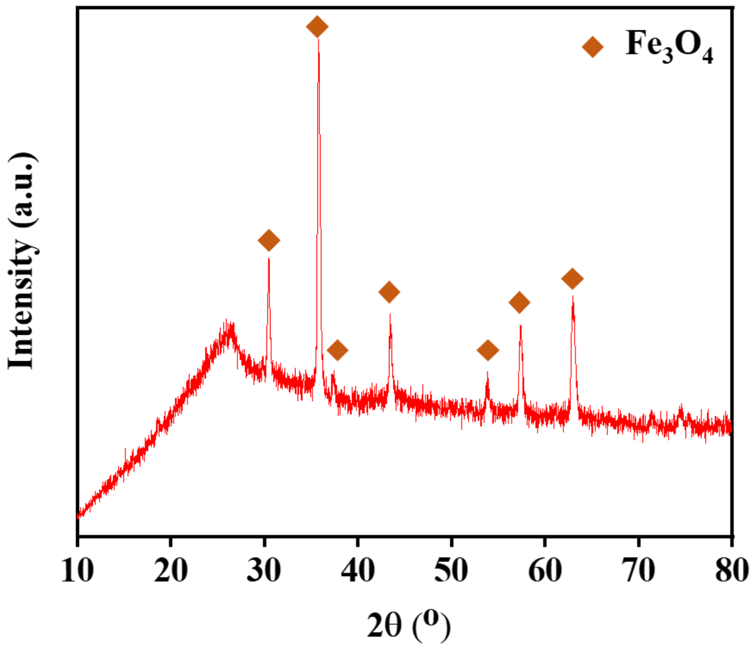

**Figure S38:** PXRD pattern of the $Fe_3O_4$ electrode after 10 h OER CA at 1.62 V vs RHE.

## References

(1) Kundu, A.; Kumar, B.; Chakraborty, B. Greigite $Fe_3S_4$-Derived α-FeO(OH) Promotes Slow O–O Bond Formation in the Second-Order Oxygen Evolution Reaction Kinetics. *J. Phys. Chem. C* **2022**, *126* (38), 16172-16186.

(2) Berry, L. G. The crystal structure of covellite, cuse and klockmannite, cuse. *Am. Mineral.* **1954**, *39* (5-6), 504-509.

(3) Donnay, G.; Donnay, J. D. H.; Kullerud, G. Crystal and twin structure of digenite,1 $Cu_9S_5$. *Am. Mineral.* **1958**, *43* (3-4), 228-242.

(4) Chakraborty, B.; Kalra, S.; Beltrán-Suito, R.; Das, C.; Hellmann, T.; Menezes, P. W.; Driess, M. A Low-Temperature Molecular Precursor Approach to Copper-Based Nano-Sized Digenite Mineral for Efficient Electrocatalytic Oxygen Evolution Reaction. *Chem. Asian J.* **2020**, *15* (6), 852-859.

(5) Momma, K.; Izumi, F. VESTA 3 for three-dimensional visualization of crystal, volumetric and morphology data. *J. Appl. Crystallogr.* **2011**, *44* (6), 1272-1276.

(6) Jain, A.; Ong, S. P.; Hautier, G.; Chen, W.; Richards, W. D.; Dacek, S.; Cholia, S.; Gunter, D.; Skinner, D.; Ceder, G.; Persson, K. A. Commentary: The Materials Project: A materials genome approach to accelerating materials innovation. *APL Mater.* **2013**, *1* (1).

(7) Downs, R. T.; Hall-Wallace, M. The American Mineralogist crystal structure database. *American Mineralogist* **2003**, *88* (1), 247-250.

(8) Merkys, A.; Vaitkus, A.; Grybauskas, A.; Konovalovas, A.; Quirós, M.; Gražulis, S. Graph isomorphism-based algorithm for cross-checking chemical and crystallographic descriptions. *J Cheminform* **2023**, *15* (1), 25.

(9) Vaitkus, A.; Merkys, A.; Grazulis, S. Validation of the Crystallography Open Database using the Crystallographic Information Framework. *J. Appl. Crystallogr.* **2021**, *54* (2), 661-672.

(10) Quirós, M.; Gražulis, S.; Girdzijauskaitė, S.; Merkys, A.; Vaitkus, A. Using SMILES strings for the description of chemical connectivity in the Crystallography Open Database. *J Cheminform* **2018**, *10* (1), 23.

(11) Grazulis, S.; Chateigner, D.; Downs, R. T.; Yokochi, A. F. T.; Quiros, M.; Lutterotti, L.; Manakova, E.; Butkus, J.; Moeck, P.; Le Bail, A. Crystallography Open Database - an open-access collection of crystal structures. *J. Appl. Crystallogr.* **2009**, *42* (4), 726-729.

(12) Gao, R.; Zhang, H.; Yan, D. Iron diselenide nanoplatelets: Stable and efficient water-electrolysis catalysts. *Nano Energy* **2017**, *31*, 90-95.

(13) Panda, C.; Menezes, P. W.; Walter, C.; Yao, S.; Miehlich, M. E.; Gutkin, V.; Meyer, K.; Driess, M. From a Molecular 2Fe-2Se Precursor to a Highly Efficient Iron Diselenide Electrocatalyst for Overall Water Splitting. *Angew. Chem. Int. Ed.* **2017**, *56* (35), 10506-10510.

(14) Mushtaq, N.; Wang, Z.; Tabassum, H.; Tahir, M.; Han, Z.; Zhu, Y.; Younas, W.; Ma, X.; Cao, C. A facile and simple microwave-assisted synthesis method for mesoporous ultrathin iron sulfide nanosheets as an efficient bifunctional electrocatalyst for overall water splitting. *Dalton Trans.* **2022**, *51* (16), 6285-6292.

(15) Le, T.-T.; Huang, S.; Ning, P.; Wang, W.; Wang, Q.; Jiang, Y.; He, Q.; Feng, J.; Hu, Z.; Chen, Z. Carbon-Decorated $Fe_3S_4$-$Fe_7Se_8$ Hetero-Nanowires: Interfacial Engineering for Bifunctional Electrocatalysis Toward Hydrogen and Oxygen Evolution Reactions. *Journal of The Electrochemical Society* **2020**, *167* (8), 086501.

(16) Chen, S.; Kang, Z.; Zhang, X.; Xie, J.; Wang, H.; Shao, W.; Zheng, X.; Yan, W.; Pan, B.; Xie, Y. Highly Active Fe Sites in Ultrathin Pyrrhotite Fe7S8 Nanosheets Realizing Efficient Electrocatalytic Oxygen Evolution. *ACS Cent. Sci.* **2017**, *3* (11), 1221-1227.

(17) Zou, X.; Wu, Y.; Liu, Y.; Liu, D.; Li, W.; Gu, L.; Liu, H.; Wang, P.; Sun, L.; Zhang, Y. In Situ Generation of Bifunctional, Efficient Fe-Based Catalysts from Mackinawite Iron Sulfide for Water Splitting. *Chem* **2018**, *4* (5), 1139-1152.

(18) Tan, Z.; Sharma, L.; Kakkar, R.; Meng, T.; Jiang, Y.; Cao, M. Arousing the Reactive Fe Sites in Pyrite (FeS2) via Integration of Electronic Structure Reconfiguration and in Situ Electrochemical Topotactic Transformation for Highly Efficient Oxygen Evolution Reaction. *Inorg. Chem.* **2019**, *58* (11), 7615-7627.

(19) Wang, G.; Jin, C.; Zhang, G.; Qian, L.; Chen, X.; Tan, J.; Wang, W.; Yin, J.; Liu, X.; Zhou, H. Surface self-reconstructed amorphous/crystalline hybrid iron disulfide for high-efficiency water oxidation electrocatalysis. *Dalton Trans.* **2021**, *50* (18), 6333-6342.

(20) Li, Z.; Xiao, M.; Zhou, Y.; Zhang, D.; Wang, H.; Liu, X.; Wang, D.; Wang, W. Pyrite $FeS_2$/C nanoparticles as an efficient bi-functional catalyst for overall water splitting. *Dalton Trans.* **2018**, *47* (42), 14917-14923.

(21) Li, H.; Wen, P.; Li, Q.; Dun, C.; Xing, J.; Lu, C.; Adhikari, S.; Jiang, L.; Carroll, D. L.; Geyer, S. M. Earth-Abundant Iron Diboride ($FeB_2$) Nanoparticles as Highly Active Bifunctional Electrocatalysts for Overall Water Splitting. *Adv. Energy Mater.* **2017**, *7* (17), 1700513.

(22) Wang, L.; Li, J.; Zhao, X.; Hao, W.; Ma, X.; Li, S.; Guo, Y. Surface-Activated Amorphous Iron Borides ($Fe_xB$) as Efficient Electrocatalysts for Oxygen Evolution Reaction. *Adv. Mater. Interfaces* **2019**, *6* (6), 1801690.

(23) Xiong, D.; Wang, X.; Li, W.; Liu, L. Facile synthesis of iron phosphide nanorods for efficient and durable electrochemical oxygen evolution. *Chem. Commun.* **2016**, *52* (56), 8711-8714.

(24) Zou, J.; Peleckis, G.; Lee, C.-Y.; Wallace, G. G. Facile electrochemical synthesis of ultrathin iron oxyhydroxide nanosheets for the oxygen evolution reaction. *Chem. Commun.* **2019**, *55* (60), 8808-8811.

(25) Zhang, X.; An, L.; Yin, J.; Xi, P.; Zheng, Z.; Du, Y. Effective Construction of High-quality Iron Oxy-hydroxides and Co-doped Iron Oxy-hydroxides Nanostructures: Towards the Promising Oxygen Evolution Reaction Application. *Sci. Rep.* **2017**, *7* (1), 43590.

(26) Babar, P. T.; Pawar, B. S.; Lokhande, A. C.; Gang, M. G.; Jang, J. S.; Suryawanshi, M. P.; Pawar, S. M.; Kim, J. H. Annealing temperature dependent catalytic water oxidation activity of iron oxyhydroxide thin films. *J. Energy Chem.* **2017**, *26* (4), 757-761.

(27) Lee, J.; Lee, H.; Lim, B. Chemical transformation of iron alkoxide nanosheets to FeOOH nanoparticles for highly active and stable oxygen evolution electrocatalysts. *J. Ind. Eng. Chem.* **2018**, *58*, 100-104.

(28) Zhang, C.; Zhang, B.; Li, Z.; Hao, J. Deep Eutectic Solvent-Mediated Hierarchically Structured Fe-Based Organic–Inorganic Hybrid Catalyst for Oxygen Evolution Reaction. *ACS Appl. Energy Mater.* **2019**, *2* (5), 3343-3351.
(29) Qian, M.; Cui, S.; Jiang, D.; Zhang, L.; Du, P. Highly Efficient and Stable Water-Oxidation Electrocatalysis with a Very Low Overpotential using FeNiP Substitutional-Solid-Solution Nanoplate Arrays. *Adv. Mater.* **2017**, *29* (46), 1704075.
(30) Wang, C.; Wang, R.; Peng, Y.; Chen, J.; Li, J. Iron tungsten mixed composite as a robust oxygen evolution electrocatalyst. *Chem. Commun.* **2019**, *55* (73), 10944-10947.
(31) Hausmann, J. N.; Beltrán-Suito, R.; Mebs, S.; Hlukhyy, V.; Fässler, T. F.; Dau, H.; Driess, M.; Menezes, P. W. Evolving Highly Active Oxidic Iron(III) Phase from Corrosion of Intermetallic Iron Silicide to Master Efficient Electrocatalytic Water Oxidation and Selective Oxygenation of 5-Hydroxymethylfurfural. *Adv. Mater.* **2021**, *33* (27), 2008823.
(32) McCrory, C. C. L.; Jung, S.; Peters, J. C.; Jaramillo, T. F. Benchmarking Heterogeneous Electrocatalysts for the Oxygen Evolution Reaction. *J. Am. Chem. Soc.* **2013**, *135* (45), 16977-16987.
(33) Shah, S. A.; Ji, Z.; Shen, X.; Yue, X.; Zhu, G.; Xu, K.; Yuan, A.; Ullah, N.; Zhu, J.; Song, P.; Li, X. Thermal Synthesis of FeNi@Nitrogen-Doped Graphene Dispersed on Nitrogen-Doped Carbon Matrix as an Excellent Electrocatalyst for Oxygen Evolution Reaction. *ACS Appl. Energy Mater.* **2019**, *2* (6), 4075-4083.
(34) Lu, X.; Zhao, C. Electrodeposition of hierarchically structured three-dimensional nickel–iron electrodes for efficient oxygen evolution at high current densities. *Nat. Commun.* **2015**, *6* (1), 6616.
(35) Chakraborty, B.; Beltrán-Suito, R.; Hausmann, J. N.; Garai, S.; Driess, M.; Menezes, P. W. Enabling Iron-Based Highly Effective Electrochemical Water-Splitting and Selective Oxygenation of Organic Substrates through In Situ Surface Modification of Intermetallic Iron Stannide Precatalyst. *Adv. Energy Mater.* **2020**, *10* (30), 2001377.
(36) Zhu, X.; Jin, T.; Tian, C.; Lu, C.; Liu, X.; Zeng, M.; Zhuang, X.; Yang, S.; He, L.; Liu, H.; Dai, S. In Situ Coupling Strategy for the Preparation of FeCo Alloys and $Co_4N$ Hybrid for Highly Efficient Oxygen Evolution. *Adv. Mater.* **2017**, *29* (47), 1704091.
(37) Zhang, B.; Zheng, X.; Voznyy, O.; Comin, R.; Bajdich, M.; García-Melchor, M.; Han, L.; Xu, J.; Liu, M.; Zheng, L.; García de Arquer, F. P.; Dinh Cao, T.; Fan, F.; Yuan, M.; Yassitepe, E.; Chen, N.; Regier, T.; Liu, P.; Li, Y.; De Luna, P.; Janmohamed, A.; Xin Huolin, L.; Yang, H.; Vojvodic, A.; Sargent Edward, H. Homogeneously dispersed multimetal oxygen-evolving catalysts. *Science* **2016**, *352* (6283), 333-337.